In situ apatite U-Pb, fission track and (U-Th)/He triple dating using a simple embedding approach

Christoph Glotzbach[1], Alexander Neely[2], Todd Alan Ehlers[3]

[1] Department of Geosciences, University of Tuebingen, Germany
[2]Arizona Geological Survey, Tucson, Arizona, USA
[3.] School of Geographical and Earth Sciences, University of Glasgow, Scotland, UK

Correspondence to: C. Glotzbach (christoph.glotzbach@uni-tuebingen.de)

Abstract. Thermo- and geochronology techniques are foundational for many studies in tectonics, petrology, and surface processes. They provide essential information about cooling histories during exhumation or burial, and sediment provenance. In the past, the application of these methods has primarily focused on using individual techniques to date separate mineral grains. More recently, analytical developments in laser-ablation geochronology have enabled the application of multiple dating techniques to an individual mineral grain (i.e., double or triple dating) to provide enhanced resolution of the mineral's thermal history or dates and, therefore, the geologic or geomorphic interpretations derived from it. However, applying multiple geochronological methods to individual grains often requires methodological compromises that can restrict their applicability. In this study, we present a simplified and robust technique for embedding apatite grains in Teflon mounts. This approach enables the combined application of U-Pb, apatite fission track, and in-situ (U-Th)/He dating. In addition, this approach preserves the ability to quantify trace-element compositions and radionuclide zoning and significantly increases the number of possible measurements per sample. The proposed analytical workflow consists of the following sequential steps: (1) grain mounting in Teflon, (2) grinding and polishing, (3) fission track etching, (4) grain selection, (5) fission track counting, (6) He measurement, (7) pit volume measurement, (8) trace element measurement, and (9) data reduction and age calculation. To ensure high data quality from in-situ (U-Th)/He analyses, we introduce a decision matrix based on four key evaluation criteria: laser pit shape, radionuclide zoning, grain geometry, and the pit–grain relationship. We apply this integrated methodology to both the well-characterized Durango apatite standard and a sample from the crystalline basement of the Odenwald, western Germany. Our results demonstrate the robustness and reliability of this approach. Specifically, we obtain in-situ (U-Th)/He ages for Durango apatite of 31.04 ± 1.04 Ma (aliquot 1, n=35) and 31.38 ± 2.53 Ma (aliquot 2, n=22), which are in excellent agreement with accepted reference ages. Apatite U-Pb and fission track ages from the same grains, completing the triple dating approach, yield ages of 31.7 ± 1.9 Ma (U-Pb concordia age) and 35.0 ± 4.4 Ma (central AFT age).
The Odenwald sample reveals a complex, multi-phase cooling history consistent with major regional geodynamic events, including Late Cretaceous doming and Eocene exhumation associated with the formation of the Upper Rhine

Graben. Importantly, our results confirm that the Teflon mounting procedure, which requires short-term heating to 300°C, does not cause measurable helium loss or reduce fission track density and track length in the near F-endmember Durango apatite, a mineral susceptible to annealing. This supports the viability of this approach for high-resolution, multi-system geo- and thermochronology thereby expanding the utility of these techniques to a broader range of geoscience applications.

1 Introduction

Advancements in UV laser-based geochronological techniques over the past two decades have significantly expanded our ability to extract complex time and thermal information from single mineral grains. These advancements have enabled routine analysis of larger sample sizes to reduce sample uncertainties, increased the resolution of derived mineral cooling histories, and expanded dating techniques to diverse detrital settings for sediment provenance determination. In particular, integrating multiple dating methods, commonly referred to as double or triple dating, offers the opportunity to reconstruct the thermal evolution or provenance history of individual crystals with unprecedented resolution. Such integrated approaches are especially powerful when applied to minerals like apatite and zircon, which can retain distinct and complementary age information over a wide range of geological temperatures.

Recent progress in UV laser-based (also called in-situ) (U–Th)/He thermochronometry has demonstrated this technique can be combined with other dating systems, such as U-Pb, Lu-Hf, and fission-track methods (e.g., Carrapa et al., 2009; Bedoya et al., 2024). These developments not only enable us to refine thermal history models and provenance interpretations but also address longstanding analytical challenges, such as detecting and correcting parent-nuclide zonation within crystals.

Despite its promise, (U–Th)/He triple dating has so far been applied in a limited number of studies. Reiners et al. (2005) were among the first to implement such an approach, combining external detector method (EDM) fission track dating and laser ablation inductively coupled plasma mass spectrometry (LA-ICP-MS) U-Pb analysis on detrital zircon. Following physical extraction from the mount, whole (or better half) grain helium was measured and whole-grain (U–Th)/He dates calculated. Carrapa et al. (2009) extended this strategy to apatite, embedding grains in epoxy for fission track and LA-ICP-MS U-Pb analysis, followed by physical extraction and helium dating of entire crystals. Similarly, Danišík et al. (2012) and Zattin et al. (2012) used variations of this workflow on detrital apatites. A more recent innovation by Bedoya et al. (2024) involved a sequential analysis of LA-ICP-MS-based fission track, U-Pb and Lu-Hf dating of single apatite grains embedded in epoxy mounts. While fission track and U-Pb analyses are made on the same spot, Lu-Hf is measured next to the spot, and therefore no extraction of grains from the mount is required (Bedoya, 2026, pers. comm.).

Epoxy, which is typically used for mount preparation, degasses under ultra-high vacuum conditions. As a consequence, alternative embedding approaches have been investigated to allow in situ (U–Th)/He dating (e.g. Boyce et al. 2006; Tripathy-Lang et al. 2013; Evans et al. 2015; Horne et al. 2016, 2019; Iwano et al. 2020). Low vapour-

pressure epoxy (Torr Seal) was successfully used for zircon, titanite and apatite in situ (U–Th)/He and U-Pb dating (Horne et al. 2016, 2019).A complex two-mounting step procedure was introduced by Boyce et al. (2006), mounting and polishing of grains in epoxy followed by physical removal of grains and pressing into non-degassing indium with the polished surface facing down. Teflon was used to embed zircons for in situ (U–Th)/He dating by Tripathy-Lang et al. (2013). Similarly, it has been successfully used for zircon (U–Th)/He and U-Pb double dating (e.g. Evans et al. 2015), while Kapton polyimide film can be used to keep grains in place during mounting. To overcome issues associated with the low strength of Teflon, Pickering et al. (2020) introduced a new embedding method based on Teflon-aluminium composite mounting.

These studies collectively confirm the reliability of in-situ (U-Th)/He approaches for both age standards and detrital samples (e.g., Boyce et al., 2006; Horne et al., 2016; Pickering et al., 2020; Tripathy-Lang et al., 2013). However, the broader application of such methods remains limited due to practical challenges associated with the (U–Th)/He dating, including the need to (i) produce flat and non-degassing mounts, (2) account for observed parent isotope zonation, and (iii) properly model the diffusional He-loss along boundaries of slowly cooled samples. Recent methodological advances have addressed many of these issues. For example, a variation of in-situ He analysis enables direct evaluation of radionuclide distribution, while improvements in thermal modelling now allow for accurate thermal history reconstruction even of small or slowly cooled apatite/zircon grains (Glotzbach and Ehlers, 2024). In this study, we present a new analytical workflow for in situ triple dating of apatite. Our method builds on previous approaches but introduces key modifications to improve efficiency and reproducibility. Most notably, we employ a standardized embedding protocol using a single Teflon foil, enabling three dating methods (U-Pb, (U-Th)/He, and fission track) to be applied sequentially to the same grain without the need for removal or remounting of grains. This streamlined technique provides a robust, high-throughput solution for simultaneously capturing crystallization and cooling histories within single apatite and also zircon grains.

2 Methods

This section outlines the analytical procedures employed for conducting fission track, (U–Th)/He, and U-Pb triple dating on apatite, as routinely performed at the University of Tübingen, Germany, and now the University of Glasgow, UK. The methods presented here follow an integrated workflow optimized for consistency and reproducibility across all three dating techniques. We provide a comprehensive description of each step, including sample mounting, apatite grain selection, fission track counting, helium measurement, pit volume determination, trace element measurement and required data reduction to calculate fission track, (U–Th)/He, and U–Pb dates (Fig. 1).

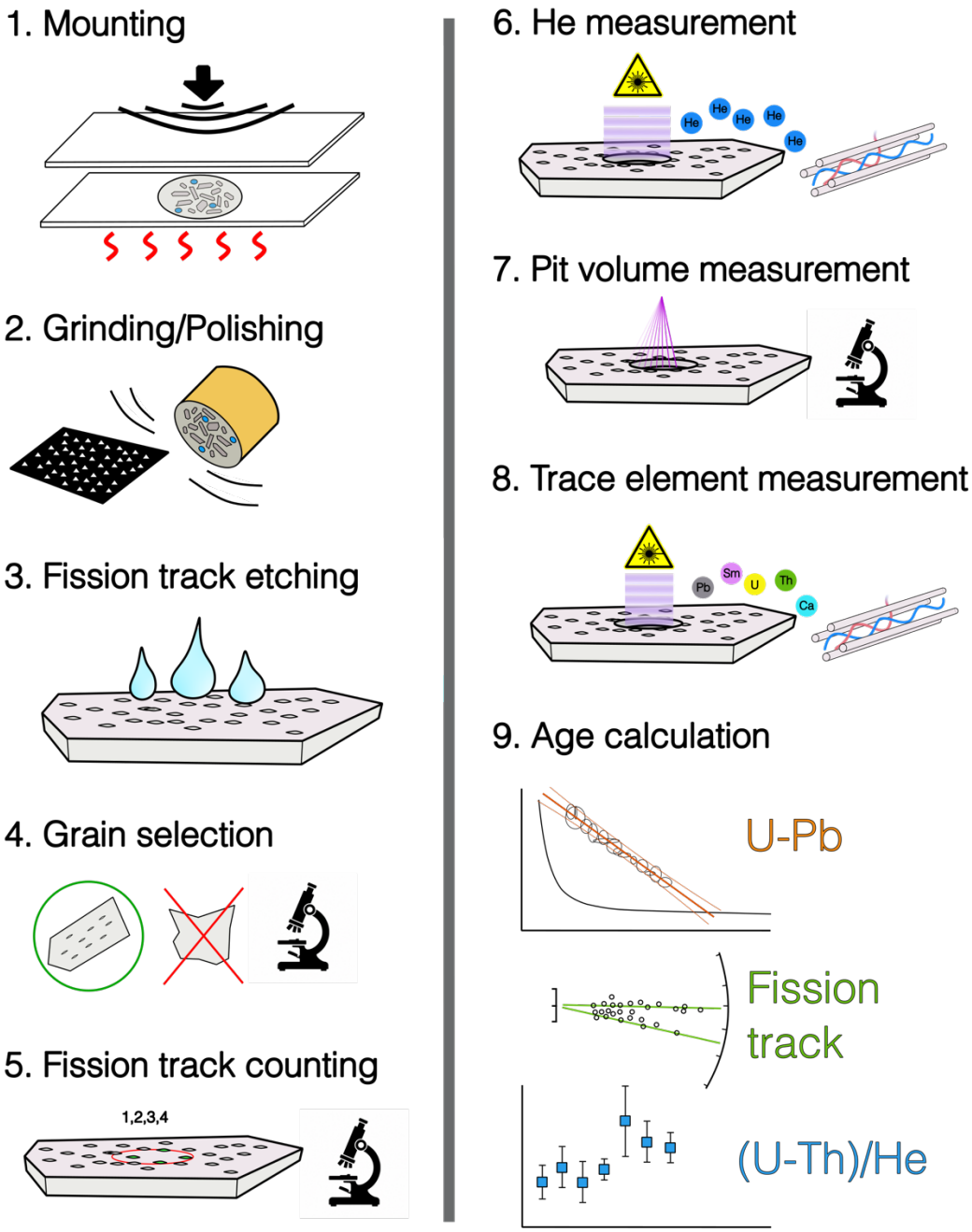

Figure 1: Schematic diagram of the analytical procedure for in-situ triple dating of apatite with the U-Pb, fission track and (U-Th)/He method.

2.1 Mount preparation

We applied a mounting procedure using 0.5 mm Teflon film (PFA FlonFilm™ 600), commonly employed for zircon FT analysis, to embed apatite grains. This approach provides compatibility with all three dating techniques, including FT visibility, ultra-high vacuum (UHV) stability, and flatness for LA analyses. The preparation steps were as follows:

1. **Initial Setup**: A clean glass slide was coated with a thin film of epoxy to fix grains in place during mounting. Note that we tested heat-resistant tape (Kapton) to fix grains in place, but it was shrinking during mounting.
2. **Bead Placement**: At least three ~150 µm diameter glass beads were arranged in a triangular formation 5-8 mm apart. These served as grinding references to ensure that more than one mean alpha-particle-stopping distance (~20 µm) was removed during polishing (following Pickering et al., 2020). Moreover, their circular geometry makes them clearly distinguishable on the mount and facilitates the automated repositioning of selected grains when transferring between analytical setups.
3. **Grain Distribution**: A few hundred apatite grains were placed within a ~2.54 cm diameter area around and between the glass beads.
4. **Teflon Film Application**: A 2.54 cm diameter Teflon disc with a thickness of 0.5 mm was placed over the grains.
5. **Mount Sealing**: A second glass slide was laid atop the Teflon film. The assembly was then heated to 295°C and pressed to embed the grains into the Teflon. Temperatures were independently measured with a Voltcraft TP-206 surface probe with a temperature accuracy of 2.5°C connected to a Voltcraft IR 800-20C thermometer. Two methods were used for the heating:
    - **Heat Plate Method**: The upper glass was preheated separately, while the lower slide with grains and Teflon was heated for ~1 minute before applying the top slide and manually pressing for ~30 s until the Teflon slightly expanded.
    - **Heat Press Method**: The glass–Teflon–glass sandwich was heated in a press (Fig. S1). After ~1 minute, pressure was applied until the Teflon slightly expanded around the grains.

    Both methods provided similar results. Note that the exact mounting temperature and time required before the mount is pressed depend on the material properties and the thickness of the used glass slides and Teflon film. See Sect. 6 for modelled time-temperature paths and the potential effect on He diffusion and fission track annealing.
6. **Cooling**: The slides were removed from the heat source and allowed to cool while maintaining pressure on the upper glass. This step ensured a flat Teflon surface, which is essential for subsequent grinding, polishing, and laser-based analyses.
7. **Grinding and Polishing**: The Teflon film was attached with double-sided tape to a round 2.54 cm diameter and 1-2 cm thick Epoxy cylinder (Fig. S1). Grinding was done with SiC adhesive paper starting with a grit of 800, 1200 and finally 2500. Subsequent polishing was performed with a Struers LaboSystem and diamant suspension starting with 6 µm, followed by 3 µm and finishing with 1 µm.

2.2 Modelling mounting-induced annealing and diffusion

The embedding method applied here using Teflon film requires heating the Teflon and mineral grains to temperatures close to 300°C, clearly exceeding the temperature at which He diffusion and fission track annealing in apatite is significant over geological timescales (e.g. Ketcham et al. 1999; Farley 2000). We therefore evaluated the effect of mounting using two different approaches: (i) forward thermal modelling of the effect of short-term heating on He diffusion and fission track annealing, and (ii) comparing fission track length distributions of samples mounted with epoxy (without heating) and Teflon (heating).

We implemented a finite difference model to simulate 1D heat conduction. The thermal parameters, initial temperatures, and boundary conditions are listed in Table 1. Note that the hotplate temperature required to lower the Teflon viscosity depends on the type of Teflon and the thickness of the glass slides. The PFA FlonFilm 600 used has a melting point of 302-310°C and is dimensionally stable until 260°C, whereas it becomes soft enough for grains to penetrate into the film at ~290°C. We set hot plate temperature to 295°C and controlled it with a thermocouple strip sensor with an accuracy of 2.5°C.

Table 1: Thermal parameters of 1D thermal model of the mounting process.

Parameter	**Value**
Hot plate temperature (°C)	295
Ambient temperature (°C)	20
Spatial resolution (mm)	0.05
Glass thermal diffusivity (m^2/s)	4.80E-07
Glass thickness (mm)	2 or 3
Teflon thermal diffusivity (m^2/s)	7.74E-08
Teflon thickness (mm)	0.5

2.3 Fission track etching

Prior to etching, sample mounts were cleaned with ethanol and compressed air to remove surface contaminants. Etching followed the protocol of Donelick et al. (2005). A glass beaker was filled with 5.5 M HNO_3 and heated to 21°C. Two mounts were held with PFA tweezers, polished surfaces facing outward, and immersed in the acid for 20 seconds. Immediately after etching, mounts were transferred to deionized water to halt the reaction.

2.4 Grain selection

Grain selection was conducted using a Zeiss Axio Imager Z2m microscope equipped with a custom Python macro, available from the associated Zenodo repository (https://doi.org/10.5281/zenodo.18979745) to streamline and standardize the process. The macro guides the user through a six-step workflow programmed to ensure the selection of suitable grains for in-situ (U-Th)/He, fission track and U-Pb dating:

1. **Sample Imaging**: The entire grain mount was imaged using the 10× objective under reflected light. A stitching routine was applied to create a high-resolution overview image of the full mount, enabling efficient navigation and documentation.
2. **Reference Point Definition**: Three easily recognizable glass beads embedded in the mount were selected to form a roughly equiangular triangle. These served as spatial reference points for accurate sample navigation and alignment during subsequent analyses.
3. **Grain Inspection**: Using the stitched overview image as a guide, individual grains were inspected at higher magnification (100× objective) under transmitted light. This allowed a detailed evaluation of each grain's geometric, surface and optical characteristics.
4. **Grain Marking**: Following inspection, grains were marked directly on the stitched overview image. Grains that met the selection criteria were marked in green, while those that failed were marked in yellow. This visual tracking system ensured that no grain was inadvertently evaluated more than once.
5. **Grain Imaging**: Suitable grains were imaged using both reflected and transmitted light to document their morphology and internal features. The vertical elevation of the polished grain surface was first identified and marked. This reference point was then used to capture (i) a high-resolution reflected light image of the grain surface, (ii) a transmitted light image stack covering the top 20 µm of the grain, and (iii) a low-resolution image with a burned-in circle marking the envisaged ablation spot. These image datasets serve two essential purposes: they are used for off-line fission track counting and enable subsequent visual inspection of the analyzed grain even after destructive laser ablation.
6. **Grain Coordinate Export**: Once >20 grains were marked as suitable for subsequent analyses, the coordinates of those grains together with reference point coordinates were exported as text files to be imported later in the excimer laser software.

The applied grain selection criteria focused on aspects such as grain size, geometry, surface quality, and purity (e.g., Flowers et al., 2023). Grains with favorable shapes (ideally euhedral) and low surface roughness were selected. Sufficient size was required to accommodate the ablation pit used in LA-MS analysis. In addition, grains were screened for inclusions, cracks, and other imperfections that could compromise dating accuracy. Note that the c-axis orientation of selected grains was not a determining selection criterion, but only those grains with a c-axis parallel to the polished grain surface were used for fission track dating.

2.5 Fission track counting

Fission track dating was performed using a custom-programmed MATLAB App (https://doi.org/10.5281/zenodo.18979745) designed to streamline and enhance the efficiency of track counting. The app enables a seamless transition between the reflected light image and the transmitted light image stack, allowing clear visualization of individual etched tracks. It also provides a visual control system to track which fission tracks have already been counted, minimizing the risk of duplicate or missed counts. Additionally, the app includes a tool to measure the diameter of etched tracks parallel to the c-axis (Dpar), with all counting statistics and Dpar values automatically stored in a structured table for further analysis and modeling.

2.6 He measurement

In-situ helium measurements on apatite grains were performed using a RESOchron system from Applied Spectra, which integrates an Alphachron He-line with a RESOlution SE 193 nm excimer laser. Samples were mounted in a UHV cell, which was pumped overnight to pressures below 1×10^{-8} torr. A low-resolution image stack of the mount was captured to relocate reference glass beads and recalculate laser pit positions, accounting for any positional shifts. This might occur because Teflon (PTFE) has a high thermal expansion coefficient of $\sim115 \times 10^{-6}\ K^{-1}$, and the mount temperature can vary between rooms or instruments during grain selection and He measurement. A 1 °C temperature change could cause a ~3 µm expansion across the 1" mount, so the temperature around the UHV cell was stabilized to near 21 °C using a Peltier-based air-air control system. Prior to ablation, each laser pit position was compared with the planned position (based on a low-resolution image, see Sect. 2.5) and adjusted if necessary. Helium was extracted using laser parameters of 30–50 µm spot size, 1.3–3 J/cm² fluence, 10 Hz repetition rate, and 2–8 seconds ablation time. Laser fluences of 1.3, 2.0 and 3.0 J/cm^2 removed 0.075, 0.100 and 0.125 µm/shot, resulting in pan-cake-shaped pits of 1–10 µm depth. The released ^{4}He was mixed with a known amount of ^{3}He, purified with a cold getter, and measured using a Pfeiffer PrismaPlus mass spectrometer. The measurement sequence included two Q-shots, multiple lineblanks, and up to five samples between blank checks. Initially, four lineblanks were run after two Q-shots due to their high ^{4}He yield (~four orders of magnitude higher than samples). Lineblank levels were monitored and measured in-between samples. The lineblank contained, on average 0.00441 ± 0.00008 ncc ^{4}He. The limit of detection (three times the standard deviation) was as low as 0.00024 ncc ^{4}He, enabling accurate dating of apatites as young as 2 million years, assuming 30 ppm eU and pit dimensions of 50 µm diameter × 5 µm depth.

2.7 Pit Volume Estimation

To convert the measured He amounts into concentrations, an accurate determination of the laser pit volumes is required. Following He analysis, the sample mount is removed from the UHV cell and transferred to a Zeiss Axio Imager Z2m microscope equipped with a Zeiss LSM900 confocal laser system. A custom Python script (https://doi.org/10.5281/zenodo.18979745) automates the volume estimation process through a series of steps:

1. **Height calibration**: The accuracy of the confocal topography measurements was evaluated using certified 5 and 10 µm step-height standards (AppNano). Measured step heights agreed with the certified values to within 1–2%. This small deviation is likely attributable, at least in part, to manufacturing tolerances or local height variations of the reference standards, and therefore does not provide a reliable basis for assigning an uncertainty to the topographic measurements. Nevertheless, the excellent agreement between the measured and certified step heights demonstrates that the confocal imaging system accurately reproduces steep vertical surfaces. Consequently, we are confident that the system provides accurate measurements of the steep walls of laser ablation pits used in this study.
2. **Sample Imaging**: The entire grain mount is imaged using a 10× objective under reflected light. A stitching routine generates a high-resolution overview image, enabling precise navigation and documentation.
3. **Reference Point Definition**: The three reference glass beads are marked to recalculate the coordinates of previously selected grains and their associated laser pits.
4. **Z-Stack Limit Definition**: For each pit, the upper and lower z-coordinates are adjusted using confocal laser scanning with the pinhole set to 1 Airy unit, ensuring accurate focus on the grain surface and pit bottom.
5. **Z-Stack Imaging**: After defining z-limits for all pits, z-stack images are collected using a 100× objective with a depth resolution of ~0.4 µm. The post-ablation surface topography is extracted from the confocal z-stack using the principle that the maximum signal intensity is reached when the surface is in focus. Although the exact algorithm is not publicly documented, the Zeiss software performs a sub-resolution interpolation by fitting the intensity peak (e.g. with a Gaussian function). This process is repeated for each pixel in x-y direction and combined into a digital elevation model (DEM) of the sample surface. Additionally, a 20× reflected light image is taken for each grain to document pit geometry and measure distances between the laser pit and grain edges required for thermal-history modelling.
6. **Pit Volume Measurement**: Using ConfoMap (Zeiss) software, pit volumes are extracted from the DEM. A macro automates this by first correcting for any tilt, defining the original grain surface, and subtracting the pit surface from the interpolated pre-ablation surface to yield the net pit volume. The pre-ablation surface was linearly interpolated from numerous x,y,z points taken a few microns around the pit.
7. **Helium Concentration Calculation**: The He amount measured from the ablation is then divided by the corresponding pit volume to derive the He concentration (e.g., in at/µm³).

This methodology ensures precise and consistent volume estimations critical for high-resolution in-situ (U-Th)/He dating.

2.8 Trace Element Measurement

Trace element concentrations in apatite were measured using a LA-ICP-MS system consisting of a RESOlution SE 193 nm excimer laser coupled to an Agilent 7900 ICP-MS. Samples, NIST SRM612 trace element reference glass and

apatite standards Durango and McClure Mountain Syenite are placed within a Laurin Technic S155 dual-volume ablation cell. To correct for instrumental drift and elemental fractionation during ablation, a sample bracketing approach was employed following the protocol of Paton et al. (2010). The trace elements analyzed included ^{29}Si, ^{31}P, ^{35}Cl, ^{43}Ca, ^{44}Ca, ^{55}Mn, ^{88}Sr, ^{89}Y, ^{139}La, ^{140}Ce, ^{141}Pr, ^{146}Nd, ^{147}Sm, ^{153}Eu, ^{157}Gd, ^{159}Tb, ^{163}Dy, ^{165}Ho, ^{166}Er, ^{169}Tm, ^{172}Yb, ^{175}Lu, ^{202}Hg, ^{204}Hg, ^{206}Pb, ^{207}Pb, ^{208}Pb, ^{232}Th and ^{238}U. Before measurement, the ICP-MS was tuned using the SRM612 glass to optimize for high sensitivity of ^{206}Pb, ^{232}Th, and ^{238}U, and in addition, targeting a $^{232}Th/^{238}U$ ratio of 1. The cell gas configuration included 350 mL/min He, 850 mL/min Ar, and a minor 0.5 mL/min N_2 addition, providing efficient aerosol transport and signal stability.

Following the approach of Evans et al. (2015), U–Pb analysis was performed using a second laser ablation (nested pit) positioned at the centre of the original He analysis pit to maintain consistent sampling conditions between standards and unknowns. This strategy is important because applied drift and downhole corrections rely on calibration using reference materials, and differences in crater geometry between standards and samples may introduce systematic biases. To ensure comparable ablation conditions for glass standards, apatite reference materials, and unknown samples, the nested pit was assigned a smaller diameter (24 or 30 µm) depending on whether the original He pit had a diameter of 30 or 50 µm, respectively. Consequently, the second ablation was performed entirely on the flat base of the initial He pit. Compared to the alternative approach of using a larger laser spot that overlaps the original He pit (e.g. Tripathy-Lang et al., 2013; Horne et al., 2016; Pickering et al., 2020). We performed the nested ablation approach, because it preserves a well-defined crater geometry, facilitates conversion of the measured signal into depth information, and enables more straightforward localization and interpretation of compositional zoning within the analysed grain.

Each analysis began with a 20-second gas background followed by 30 seconds of ablation at a fluence of 3 J/cm². The resulting data were processed using an in-house MATLAB App (https://doi.org/10.5281/zenodo.18979745), which carried out:

- Automatic removal of data gaps
- Manual or automatic outlier rejection based on a running standard deviation threshold
- Background subtraction
- Manual or automated selection of integration intervals
- Calculation of trace element concentrations using ^{43}Ca (or ^{44}Ca) as the internal standard

Assumed CaO concentrations were 11.9% for SRM612 (Jochum et al., 2011) and 55.6% for apatite, based on its stoichiometric composition. Calibration curves were interpolated between 5-6 subsequent SRM612 measurements to account for temporal drift. Final concentrations were calculated following the method of Longerich et al. (1996).

2.9 U-Pb age calculation

U–Pb age calculations were performed using the in-house MATLAB App (https://doi.org/10.5281/zenodo.18979745). Raw isotope ratios, such as $^{206}Pb/^{238}U$ were corrected for drift in mass ratios and downhole fractionation following the approach of Paton et al. (2010) by employing the Durango apatite age standard. Common Pb corrections were carried

out either by directly measuring ^{204}Pb, in cases where ^{204}Pb counts were significant and indistinguishable from the background (as in apatite), or by applying a ^{207}Pb or ^{208}Pb correction following Williams (1998) was applied. This method relies on a common Pb evolution model, for which we used the Stacey and Kramers (1975) model. Final sample ages were derived from either a Tera-Wasserburg diagram or following the ^{207}Pb or ^{208}Pb common Pb correction derived from a Concordia plot. It is important to note that prior chemical etching of fission tracks may affect U–Pb dating by removing material and thereby lowering grain density, particularly at the surface and in areas with high spontaneous fission track densities. However, most etched tracks were removed during the first ablation step for He measurement, and Abdullin et al. (2021) demonstrated that U–Pb dating is not significantly influenced by prior etching.

2.10 Fission track age calculation

Fission-track ages were calculated using the **ζ**-based LA-ICP-MS approach (Donelick et al. 2005) with Durango apatite as the primary age standard. Kinetic properties of apatite crystals were determined by measurement of Dpar values (mean of 4 per crystal), complemented by chlorine measurements using LA-ICP-MS and Durango apatite for calibration (e.g. Chew et al. 2013).

Repeated measurements of 20 Durango shards measured during 15 different LA-ICP-MS sessions with in total 72 individual measurements yield a zeta (**ζ**) of 2479±33 calculated with:

$$\zeta = \frac{e^{\lambda_d t_{std}} - 1}{\lambda_d \rho_s / U} \qquad \text{Eq. 1}$$

where $\boldsymbol{\lambda}_d$ is the total decay constant of ^{238}U [1/Myr], t_{std} is the age of Durango apatite of 31.44±0.18 Ma (McDowell et al. 2005), ρ_s is the spontaneous fission track density [tracks/cm^2] and U is the Uranium concentration [g/g].

2.11 (U—Th)/He age calculation

In-situ (U–Th)/He ages were calculated following the approach of Meesters and Dunai (2005), using the measured U, Th, Sm, and He concentrations for each analysis. Concentrations were converted to atoms/μm^3 assuming a density of 3.19 g/cm^3. Uncertainties associated with the U, Th, Sm, and He measurements were propagated through the age calculation using a Monte Carlo approach. Pit volume uncertainties were not considered. For each analysis, 1,000 ages were generated by randomly sampling the input parameters from distributions defined by their respective analytical uncertainties. The reported in-situ (U–Th)/He age corresponds to the mean of the resulting age distribution, and its uncertainty is given by the standard deviation of the 1,000 Monte Carlo realizations.

3 Sample Details

We applied the triple dating approach to a Durango apatite standard and a sample from the basement of the Odenwald, Germany (22BGE055T). Two Durango aliquots with 35 (Durango1) and 25 (Durango2) crystal shards, and 22 grains from 22BGE055T were analysed. The Durango apatite comes from the skarn deposit of the Cerro de Mercado iron mine in Durango, Mexico. Apatites formed in a high-temperature hydrothermal environment linked to the eruption of intermediate to felsic ignimbrites sourced from the Chupaderos caldera (e.g. McDowell et al. 2005). While the Durango apatite is a challenging standard for U-Pb dating due to its young age, high Th/U ratio, and variable amounts of common Pb, it is nonetheless widely used as a primary age standard for fission track and (U–Th)/He dating. ID-TIMS apatite U-Pb analyses yielded an age of 32.716 ± 0.061 Ma, although this likely overestimates the true crystallization age due to excess ^{206}Pb (Paul et al. 2021). The latter is mostly the product of the ^{238}U decay chain, but can also be produced in a small amount from ^{230}Th directly, which is incorporated in minerals with a high Th/U ratio, such as Durango apatite (Paul et al. 2021). Therefore, we assume that the indirect ^{40}Ar/^{39}Ar dates of the stratigraphically bracketing ignimbrite (31.44 ± 0.18 Ma; McDowell et al. 2005) more reliably reflect the crystallization age of Durango apatite. Since the Durango apatite formed near the surface, we expect that our triple dating approach will yield very similar ages. Analyses were conducted on 100-200 µm shards of a crushed gem-quality Durango apatite crystal.

Sample 22BGE055T was collected from the crystalline basement of the Odenwald, which, along with the Black Forest, forms the uplifted eastern shoulder of the Upper Rhine Graben. This sample was taken at latitude 49.57254°N and longitude 8.66981°E north of Weinheim, Germany, from the Lower Carboniferous Weschnitz pluton, and is granodioritic in composition. Previous K–Ar dating on biotite and hornblende yielded ages of 320–330 Ma (Kreuzer and Harre 1975), and petrographic analyses reveal a predominantly mantlederived source of melts (e.g. Will et al. 2021). Following the emplacement at pressures of 4.5–5 kbar and depths exceeding 15 km (Stein and Dietl 2001), the crystalline basement was largely leveled and exposed to Earth's surface prior to the Upper Permian marine transgression. Subsequent subsidence continued at least until the Middle Jurassic, accompanied by deposition of up to 1500 m of various sedimentary rocks (Wagner 1969). Large-scale doming resulted in complete removal of the sedimentary cover in the northern Odenwald during Eocene times, which is recorded in the buried Upper Rhine graben Eocene planation surface (Ziegler 1990) The southern Odenwald remained partly buried, as evidenced by the emplacement of the Katzenbuckel at ~68–70 Ma (Schmitt et al. 2007) into Middle Jurassic rocks (Wagner 1969). Final exhumation of the southern Odenwald likely initiated during the Middle Oligocene, driven by tectonic activity along the Upper Rhine Graben (Wagner 1969). Grain selection mostly followed the above criteria (Sect. 2.5), however, some subhedral grains were selected that were suitable for U-Pb and AFT dating, but not ideal for (U-Th)/He dating. In total 22 grains with grain radii from 32 to 128 µm were analysed.

4 Results

4.1 Mounting induced annealing and diffusion

The 1D thermal diffusion modelling revealed that the Teflon film approached the hot plate temperature after 60 s for 2 mm thick glass slides, whereas it took 90 s for 3 mm thick glass slides (Fig. S2A,B). Cooling to ambient temperature is comparable assuming efficient heat transfer (ventilation) from the glass slides (Fig. S2C,D).

The modelled time-temperature (tT) paths at the locations of the embedded apatite grains on the lower side of the Teflon film were extracted from the model and used as input for forward thermal modelling of apatite fission-track and (U-Th)/He data. Since fission track annealing is length-dependent and the track stability against annealing increases as tracks become shorter we tested two scenarios without (1-) and with (2-) pre-mounting track shortening (Fig. 2). Both scenarios assume that the temperature of the theoretical apatite grain was 20°C at 10 Ma and heating during mounting occurred at 3-4 minutes before the end of the model to allow cooling to room temperature (Fig. 2). Scenarios 1- assumes that the pre-mounting temperature stayed at 20°C, while linear heating and cooling to 80°C at 5 Ma was used in scenarios 2- to reduce track length before mounting (Fig. 2). These pre-mounting tT paths were combined with modelled mounting tT paths for 2 (M2) and 3 mm (M3) thick mounting glasses and mounting temperatures of 295 to 320°C (Fig. 2).

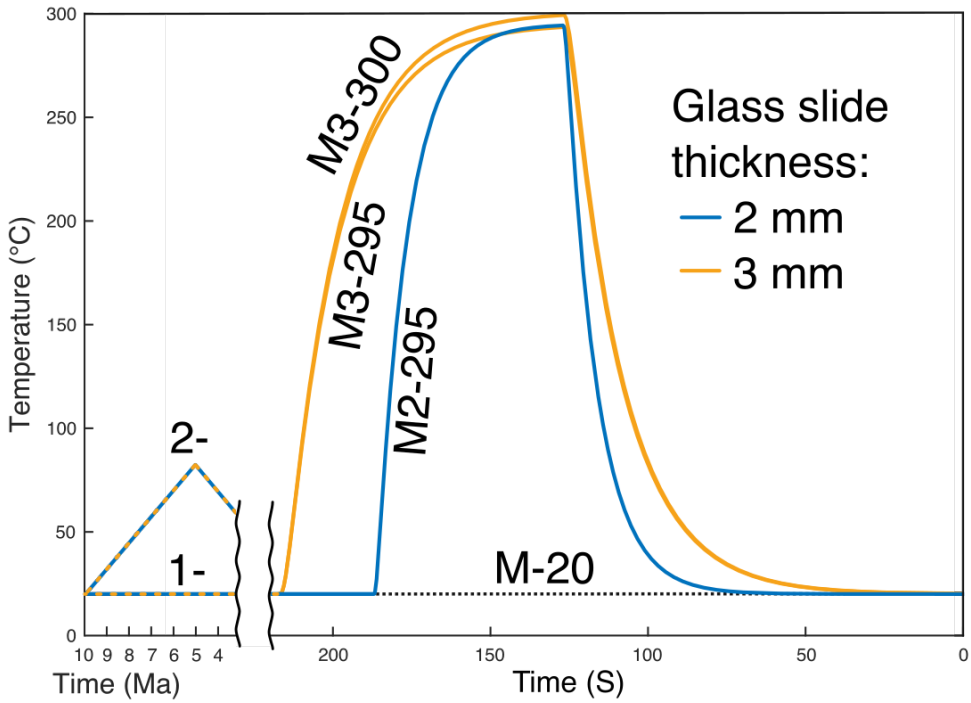

Figure 2: Time-temperature (tT) path used to model the impact of our mounting protocol on apatite fission track annealing and He diffusion. Model scenarios include no pre-mounting heating (1-) and linear heating to 80°C at 5 Ma (2-), followed by mounting tT paths for glass thicknesses of 2 and 3 mm (M2, M3) and hot plate/press temperatures of 295 to 320°C. For comparison an unrealistic mounting temperature of 20°C is assumed (scenarios M-20).

During mounting, the modelled temperature temporarily matches the hot plate temperature, remaining above 250°C for approximately 45 seconds with 2 mm glass and about 60 seconds with 3 mm glass. This results in minor apatite fission track annealing and negligible helium diffusion for Durango-type apatite chemistry (Table 2). Without pre-mounting fission-track annealing (scenario 1-), AFT ages are about 1% younger at a mounting temperature of 295°C than in unmounted samples. This discrepancy increases to 2% at 305°C and exceeds 3.6% at 320°C. The length reduction of unannealed fission tracks is, on average, less than 0.1 μm - at the threshold of detectability - and does not significantly affect modelled cooling histories. Similarly, apatite (U-Th)/He ages are negligibly affected by the mounting process (Table 2).

In Scenario 2, where pre-mounting heating causes partial fission-track annealing, subsequent mounting at temperatures below 310°C results in less than 0.5% additional fission-track annealing and less than 0.7% He diffusion. Notably, the mean track length (MTL) remains virtually unchanged for mounting temperatures below 305°C. These findings indicate that the Teflon-based mounting procedure has no significant impact on apatite fission-track or (U-Th)/He data when mounting is performed quickly and at temperatures not exceeding ~300°C.

Table 2: Modelled apatite fission track (AFT) age, mean track length (MTL), (U-Th)/He (AHe) age and total He for various (pre-) mounting scenarios for Durango-type apatite chemistry and annealing and diffusion models of Ketcham et al. (2007) and Flowers et al. (2009).

Scenario	**Hot Plate Temp (°C)**	**AFT age (Ma)**	**MTL (μm)**	**AHe age (Ma)**	**Total He (mol/g)**
1-M-20	20	10.20	14.54±1.05	9.90	0.8824
1-M2-295	295	10.10	14.47±1.04	9.90	0.8819
1-M3-295	295	10.10	14.46±1.04	9.90	0.8818
1-M3-300	300	10.10	14.45±1.04	9.90	0.8817
1-M3-305	305	10.00	14.38±1.04	9.89	0.8814
1-M3-310	310	9.97	14.32±1.04	9.89	0.8812
1-M3-320	320	9.83	14.16±1.04	9.88	0.8805
2-M-20	20	9.01	13.27±1.43	6.13	0.5460
2-M2-295	295	9.01	13.26±1.41	6.13	0.5459
2-M3-295	295	9.00	13.26±1.40	6.13	0.5458
2-M3-300	300	9.00	13.25±1.39	6.13	0.5458
2-M3-305	305	8.98	13.22±1.38	6.09	0.5428
2-M3-310	310	8.96	13.20±1.37	6.09	0.5427
2-M3-320	320	8.92	13.15±1.33	6.09	0.5426

To support the modelling approach, an experiment was conducted using the same sample mounted in two different ways: in epoxy without heating and in Teflon with heating. Fission track length measurements were then performed.

The sample used was from the Upper Triassic Stubensandstein formation in southwestern Germany (sample 22BGE032T), sharing a similar cooling history as sample 22BGE055T.

In the epoxy-mounted sample, 103 confined fission tracks were measured, yielding a relatively broad track length distribution with a c-axis corrected mean track length (MTL) of 13.12 ± 1.34 µm. In the Teflon-mounted sample, also with 103 measured tracks, the MTL was 13.09 ± 1.05 µm. These results support the modelling outcome, confirming that the Teflon mounting protocol leads to negligible shortening of apatite fission tracks.

4.2 Trace Element Composition

The trace element composition of Durango apatite is characterized by distinctly elevated light rare earth element (LREE) concentrations relative to heavy rare earth elements (HREE), a pronounced negative Eu anomaly, and high Th/U ratios (Fig. 3A). According to the classification scheme of O'Sullivan et al. (2020), these characteristics suggest a source in the broad mafic I-type granitoids (IM) field that also includes non-peraluminous granitoids and rhyolite (Fig. 3C). Slight compositional differences observed between the Durango1 and Durango2 aliquots are attributed to moderate zoning, as is common in Durango apatite (e.g. Chew et al. 2016).

In contrast, apatite grains from sample 22BGE055T display a broader compositional range, particularly in HREE concentrations, which vary by more than an order of magnitude (Fig. 3B). These grains show consistently low Th/U ratios and are marked by a significant negative Sr anomaly. Most grains exhibit only moderately higher LREE ratios relative to HREE, and four grains stand out with a strong negative Eu anomaly, these same grains also record the most pronounced Sr depletion. The presence or absence of a Eu anomaly is interpreted to reflect the timing of feldspar crystallization relative to apatite. Eu exist in two oxidation states (2+ and 3+) in magmatic systems and Eu^{2+} is similar in charge and has a quite similar ionic radius to Ca^{2+}, and is therefore largely removed from the melt through crystallisation of feldspar (e.g. Holder et al. 2020). Apatite crystallizing after feldspar will therefore record a negative Eu anomaly, whereas early-crystallizing apatite typically lacks this feature (e.g. Larsen 2002). Classification based on REE spider diagram patterns (Fig. 3D) suggests that apatite in sample 22BGE055T most likely originate from I-type granitoids and high-grade metamorphic rocks, consistent with a dominantly mantle-derived I-type magmatic source (e.g. Will et al. 2021).

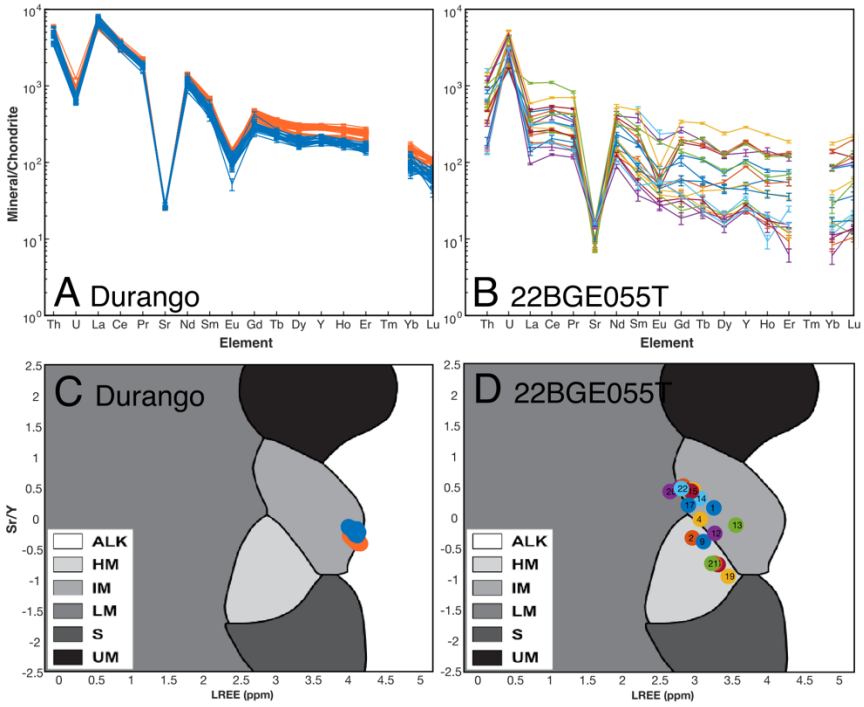

Figure 3: A,B) Chondrite-normalised rare earth element (REE) plus U, Th and Sr multi-element plot (spider diagram) of Durango apatite (red – Durango1, blue – Durango2) and sample 22BGE055T. Gaps represent non-analysed elements. C,D) Sr/Y vs. ∑LREE biplot of Durango apatite (red – Durango1, blue – Durango2) and 22BGE055T trace element results. Background grey colours represent the classification proposed O'Sullivan et al. (2020): ALK – alkali-rich igneous, HM – partial-melts/leucomes/high-grade metamorphic, IM – mafic I-type granitoids and mafic igneous, LM – low- and medium-grade metamorphic and metasomatic, S – S-type granitoids and high-aluminum saturation index felsic I-types, UM – ultramafic rocks including carbonatites, lherzolites and pyroxenites.

4.3 U-Pb Age

The U-Pb analyses of Durango1 apatite exhibit a narrow range in common Pb composition, as evidenced by the limited range of data points in the Tera-Wasserburg diagram (Fig. 4A). This restricted variation indicates a uniform common Pb component across the analysed shards and prevents the construction of a well-constrained discordia line and obscures a meaningful lower intercept age. The common Pb composition of Durango apatite has been recently determined by ID-TIMS, suggesting an y-intercept of 0.862 ± 0.004 (Paul et al. 2021). With this assumption, we could derive a lower intercept age for sample Durango1 of 31.5 ± 3.5 Ma. Following a ^{207}Pb-based common Pb correction, all Durango analyses yield a common Concordia age of 31.7 ± 1.9 Ma (Fig. 4B). Additionally, the concordant U-Pb data (defined here as 80-120% concordance) yield an average ^{208}Pb/^{232}Th age of 33.0 ± 3.1 Ma. All derived U-Pb ages agree well with the independently constrained crystallization age of 31.44 ± 0.18 Ma from stratigraphically bracketing ignimbrites (McDowell et al. 2005). U-Pb data for sample Durango1 were derived with a laser pit diameter of 30 µm, while a 24 µm laser pit diameter was used for Durango2, resulting in significantly higher uncertainties. For instance, concordant ^{208}Pb/^{232}Th measurements yield an average age of 34.0 Ma with a standard deviation of 6.2 Ma,

which is twice the standard deviation obtained for comparable measurements with a laser pit diameter of 30 µm (Durango1).

In contrast, apatite grains from sample 22BGE055T contain a more significant and variable component of common Pb. Common Pb creates scatter in the Tera-Wasserburg diagram and preventing direct age determination through regression (Fig. 4C). After common Pb correction (based on the ^{207}Pb correction method), the subset of analyses with concordant U-Pb ratios yields an average ^{206}Pb/^{238}U age of 290.1 ± 25.0 Ma, while the weighted concordia age is 298.5 ± 7.2 Ma (Fig. 4D). These U-Pb ages are slightly younger than previously reported K-Ar biotite and hornblende cooling ages of 320–330 Ma (Kreuzer and Harre 1975). The typical closure of the U-Pb system in apatite has been determined at 350-570°C (Cherniak et al. 2010), and is therefore somewhat higher than that of the K-Ar biotite system modelled at 280-345°C for cooling rates of 1-100°C/Myr (Harrison et al. 1985). Potential reasons for young apatite U-Pb compared to K-Ar ages are (i) regional variations in ages or (ii) sample-specific variations in closure temperatures. For instance, diffusion of Pb from U-rich to U-low zones can significantly increase whole-grain and in-situ apatite U-Pb spread (e.g., Paul et al., 2019). Regardless, available ages are similar, suggesting rapid post-emplacement cooling, consistent with other basement highs in Central Europe, such as the Black Forest (Timar-Geng et al. 2006) and the Thuringian Forest (Thomson and Zeh 2000).

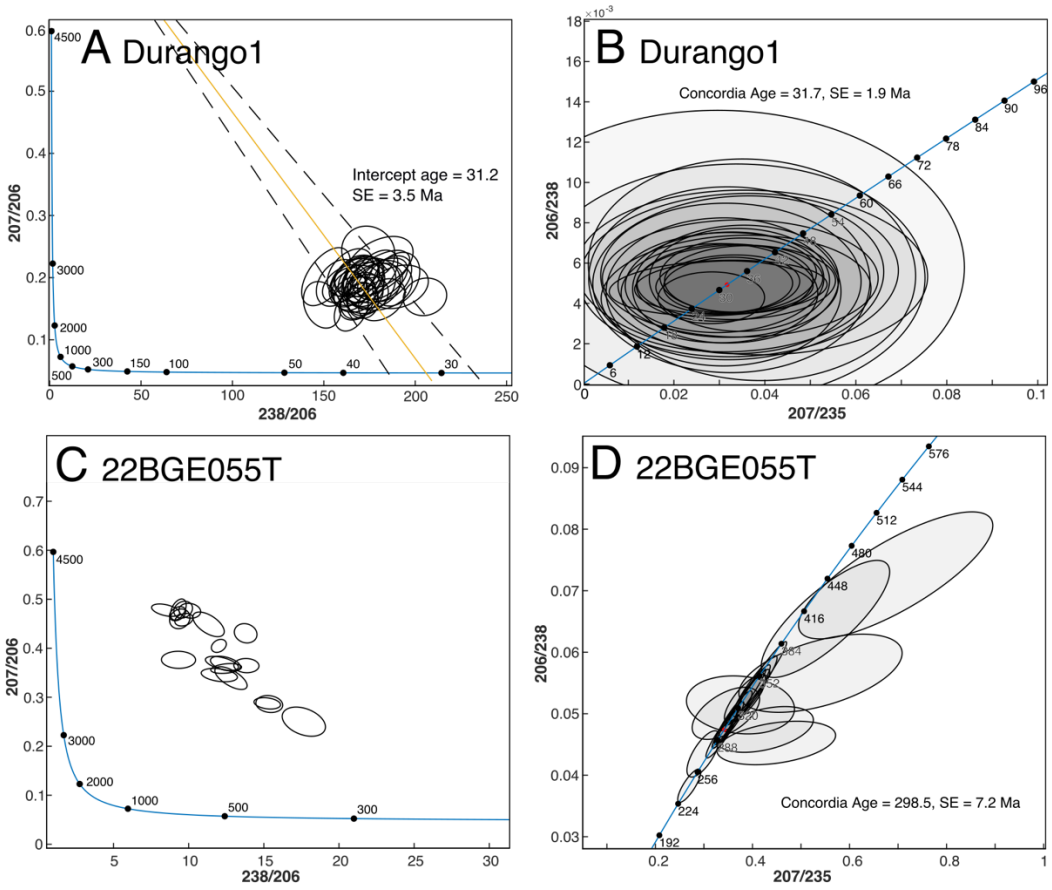

Figure 4: Apatite U-Pb data for Durango1 and 22BGE055T. A,C) Tera-Wasserburg diagram. B,D) Concordia diagram with derived lower intercept, concordia age and standard error (SE). Note that single grain data of

22BGE055T does not define a statistically significant linear trend, preventing the derivation of a meaningful lower intercept in the Tera-Wasserburg diagram.

4.4 Fission Track Age

Fission track analyses were conducted on apatite samples Durango2 and 22BGE055T, with only a subset of selected grains successfully dated due to the method's strict requirements for c-axis parallel orientation and undisturbed internal grain surfaces (Table 3). The Durango2 apatite, characterized by a low uranium concentration averaging 13.1±1.3 ppm and a relatively small counting area (30 μm diameter), yielded a low number of counted tracks (4±2 on average per counted area). Consequently, individual ages show wide variation, ranging from 0.0±10.3 Ma to 61.0±21.6 Ma. The resulting central age of 35.0 ± 4.4 Ma overlaps with the independently determined $^{40}Ar/^{39}Ar$ age of 31.44±0.18 Ma for Durango apatite (McDowell et al., 2005).

In contrast, sample 22BGE055T displays significantly higher uranium concentrations (59.7±24.5 ppm), which, along with older apparent ages, led to 17±6 tracks counted in average on the 30 μm laser footprint. Single spot/grain ages for this sample range from 37.8±13.4 Ma to 129.3±31.6 Ma, with a central age of 92.1±5.8 Ma, well within the established AFT age range for the Odenwald region (~70–105 Ma; Wagner, 1969). Additionally, 68 confined track lengths were measured for 22BGE055T, yielding relatively short tracks with a mean track length (MTL) of 12.61±1.20 μm (Fig. 8C), indicative of substantial annealing.

Table 3: Apatite fission track results of Durango2 and 22BGE055T.

Sample	Pit diameter (μm)	Laser fluence (J/cm^2)	Ablation time (s)	Ns	Nd (tracks/cm^2)	U (ppm)	U 1σ (ppm)	Dpar (μm)	Age (Ma)	Age 1σ (Ma)
Durango2										
Grain01	24	3	30	3	1.53E+05	12.28	0.06	1.54	30.2	17.4
Grain02	24	3	30	3	1.53E+05	13.71	0.05	1.71	27.0	15.6
Grain03	24	3	30	1	5.09E+04	13.68	0.05	1.70	9.0	9.0
Grain04	24	3	30	5	2.04E+05	15.13	0.06	1.65	40.8	18.3
Grain05	24	3	30	7	3.06E+05	13.82	0.05	1.62	62.4	23.6
Grain06	24	3	30	not c-axis parallel		11.82	0.05	-	-	-
Grain07	24	3	30	4	1.53E+05	11.94	0.05	1.59	41.3	20.7
Grain08	24	3	30	5	1.53E+05	11.68	0.05	1.59	52.7	23.6
Grain09	24	3	30	2	5.09E+04	12.16	0.05	1.61	20.3	14.4
Grain10	24	3	30	2	1.02E+05	12.08	0.05	1.88	20.4	14.5
Grain11	24	3	30	0	0.00E+00	12.03	0.05	1.62	0.0	10.3
Grain12	24	3	30	6	2.55E+05	11.86	0.05	1.56	62.3	25.5
Grain13	24	3	30	dislocations		15.23	0.06	-	-	-
Grain14	24	3	30	dislocations		15.22	0.06	-	-	-
Grain15	24	3	30	not c-axis parallel		13.42	0.06	-	-	-
Grain16	24	3	30	4	2.04E+05	13.24	0.05	1.62	37.3	18.7
Grain17	24	3	30	4	1.53E+05	13.29	0.05	1.48	37.1	18.6
Grain18	24	3	30	3	1.53E+05	12.51	0.05	1.63	29.6	17.1
Grain19	24	3	30	dislocations		16.49	0.06	-	-	-
Grain20	24	3	30	dislocations		16.17	0.06	-	-	-
Grain21	24	3	30	3	1.02E+05	11.92	0.05	1.51	31.1	18.0
Grain22	24	3	30	dislocations		16.02	0.06	-	-	-
Grain23	24	3	30	8	4.07E+05	16.15	0.07	1.40	61.0	21.6
Grain24	24	3	30	3	1.53E+05	13.90	0.04	1.67	26.6	15.4
Grain25	24	3	30	4	1.53E+05	14.88	0.06	1.60	33.2	16.6
Average				***4±2***	***1.61±0.95E05***	***13.1±1.3***		***1.61±0.10***	***35.0±4.4***	
22BGE055T										
Grain01	24	3	30	17	1.71E+06	31.8	0.1	1.64	129.3	31.6
Grain02	24	3	30	not c-axis parallel		42.0	0.2	-	-	-
Grain03	24	3	30	18	1.70E+06	-	-	1.63	-	-
Grain04	24	3	30	not c-axis parallel		83.9	0.4	-	-	-
Grain05	24	3	30	14	2.17E+06	52.8	0.3	1.49	98.9	26.6
Grain06	24	3	30	21	1.87E+06	35.5	0.2	1.74	127.0	27.9
Grain07	24	3	30	9	1.57E+06	47.2	0.2	1.56	80.4	26.9
Grain08	24	3	30	24	3.86E+06	96.3	0.5	1.64	96.7	19.9
Grain09	24	3	30	18	1.98E+06	47.8	0.2	1.65	99.6	23.6
Grain10	24	3	30	19	2.79E+06	58.6	0.3	1.54	114.7	26.5
Grain11	24	3	30	9	1.47E+06	32.7	0.2	1.60	107.9	36.1
Grain12	24	3	30	8	1.56E+06	100.3	0.6	1.62	37.8	13.4
Grain13	24	3	30	21	1.62E+06	53.6	0.3	1.53	72.8	16.0
Grain14	24	3	30	6	7.38E+05	30.3	0.2	1.36	58.9	24.1
Grain15	24	3	30	17	1.53E+06	35.8	0.2	1.56	103.0	25.2
Grain17	24	3	30	18	2.01E+06	61.2	0.3	1.56	79.2	18.8
Grain18	24	3	30	15	2.22E+06	66.1	0.4	1.54	81.0	21.0
Grain19	24	3	30	25	4.86E+06	111.2	0.6	1.72	105.1	21.2
Grain20	24	3	30	10	2.13E+06	62.7	0.4	1.60	81.9	26.0
Grain21	24	3	30	26	3.25E+06	83.6	0.5	1.53	93.6	18.5
Grain22	24	3	30	27	2.97E+06	67.7	0.4	1.68	105.7	20.5
Average				***17±6***	***2.21±0.97E06***	***59.7±24.5***		***1.59±0.09***	***92.1±5.8***	

4.5 (U-Th)/He Age

In-situ (U-Th)/He age measurements were conducted on three samples: Durango1, Durango2, and 22BGE055T, yielding consistent results that validate the analytical approach and highlight the influence of grain-specific factors on

age variability (Table 4). Exclusion of measurements (italic font) is based on exclusion criteria related to the laser pit and grain geometry, element zoning and pit-grain relationship that are detailed in section 5.2.

Durango1 was measured with variable laser fluence (1.3-3 J/cm^2) and ablation times (2-8 s), creating variable laser pits (Table 4). Accordingly, He concentrations varied from 0.0034 to 0.0277 ncc, approximately 0.75 to 6 times the blank level, resulting in standard deviations between 8.6% and 1.1%, respectively (Table 4). The calculated He concentrations varied from 5.39 to 7.63×10^{-20} mol/µm³, with corresponding Sm, Th, and U concentrations spanning 232–320 ppm, 357–497 ppm, and 16–26 ppm, respectively. The resulting single-spot in-situ ages for Durango1 ranged from 28.9 to 34.7 Ma, with an average age of 31.04 ± 1.04 Ma (n = 35). The range of applied laser fluences and size of resulting ablation pits had no visible impact on the resulting ages.

Durango2 yielded measured He concentrations between 0.0111 and 0.0199 ncc, equating to approximately 15 to 28 times the blank level, with low standard deviations of 2.8% to 1.1% (Table 4). He concentrations for Durango2 varied from 3.83 to 6.80×10^{-20} mol/µm³, while Sm, Th, and U concentrations were 139–353 ppm, 250–442 ppm, and 11–16 ppm, respectively. Single-grain ages from 22 spot analyses ranged from 23.8 to 34.5 Ma, with an average age of 31.38 ± 2.53 Ma. Notably, the derived in-situ ages for Durango1 and Durango2 are in excellent agreement with the independently determined $^{40}Ar/^{39}Ar$ age of 31.44±0.18 Ma and the whole-grain apatite age of 31.02±1.01 Ma (McDowell et al., 2005).

For sample 22BGE055T, the measured He content of individual laser-ablation pits ranged from 0.0033 to 0.0167 ncc, corresponding to 4 to 20 times the line blank level, with standard deviations of 1.6% to 5.7% (Table 4). Laser pits with diameters of 30 µm yielded pit volumes of 3237 to 3987 µm³, resulting in He concentrations of 0.41 to 1.87×10^{-19} mol/µm³. Associated Sm, Th, and U concentrations varied widely from 15–296 ppm, 11–149 ppm, and 30–123 ppm, respectively. The resulting in-situ (U-Th)/He ages for 22BGE055T displayed significant variation, ranging from 36.2 ± 10.0 to 106.8 ± 2.5 Ma (Fig. 5). Ages do not reveal any relation with eU, instead the large age range is attributed to factors such as grain size (e.g., Grain07 with radius of 32 µm), ambiguous grain geometry (e.g., Grain04 is a broken grain), and pronounced element zoning (e.g., Grain12 and Grain21). Excluding grains with these complexities yields a mean age of 71.5 ± 21.5 Ma, compared to 73.0 ± 19.0 Ma when all grains are included. The greater dispersion in ages relative to the Durango standards is expected, given the variations in grain size, radionuclide concentrations, and the more complex thermal history of sample 22BGE055T.

Table 4: In-situ apatite (U-Th)/He results of Durango1, Durango2 and 22BGE055T.

Sample	Pit diameter (μm)	Laser fluence (J/cm²)	Ablation time (s)	4He (ncc)	4He 1σ (%)	4He (mol)	4He 1σ (mol)	Pit volume (μm³)	Pit volume 1σ (μm³)	4He (mol/μm³)	4He 1σ (mol/μm³)	Sm (ppm)	Sm 1σ (ppm)	Th (ppm)	Th 1σ (ppm)	U (ppm)	U 1σ (ppm)	eU (ppm)	Age (Ma)	Age 1σ (Ma)	Laser pit	Element zoning	Grain geometry	Pit-Grain relation
Durango1																								
Grain01	50	1.3	4	0.0068	5.8	3.03E-16	1.77E-17	5123	3	5.91E-20	1.43E-21	306.4	10.9	375.0	8.3	19.1	0.4	107.3	31.6	1.0	0	0	na	0
Grain02	50	1.3	2	0.0039	3.8	1.75E-16	6.59E-18	2628	43	6.64E-20	1.69E-21	306.3	10.7	384.4	8.4	19.4	0.4	109.7	34.7	1.1	0	0	na	0
Grain03	50	1.3	6	0.0096	3.2	4.26E-16	1.35E-17	7222	4	5.90E-20	1.05E-21	305.9	10.8	392.8	8.6	19.1	0.4	111.4	30.4	0.8	0	0	na	0
Grain04	50	1.3	2	0.0034	8.3	1.52E-16	1.26E-17	2738	6	5.54E-20	1.60E-21	247.9	8.9	368.3	8.1	17.8	0.4	104.3	30.5	1.0	0	0	na	0
Grain05	50	1.3	4	0.0066	6.0	2.94E-16	1.75E-17	5281	2	5.57E-20	1.36E-21	250.9	9.0	371.4	8.2	17.8	0.4	105.1	30.4	1.0	0	0	na	0
Grain06	50	1.3	6	0.0092	2.7	4.10E-16	1.11E-17	7381	11	5.55E-20	9.20E-22	239.1	8.6	364.6	8.0	17.4	0.4	103.1	30.9	0.8	0	0	na	0
Grain07	50	1.5	8	0.0137	2.5	6.11E-16	1.53E-17	11253	20	5.43E-20	8.65E-22	243.3	8.8	368.0	8.1	17.3	0.4	103.8	30.0	0.7	0	0	na	0
Grain08	50	2.0	8	0.0169	2.2	7.55E-16	1.63E-17	13695	23	5.51E-20	8.16E-22	244.2	8.9	359.0	8.0	17.2	0.4	101.5	31.2	0.7	0	0	na	0
Grain09	50	2.5	8	0.0207	1.7	9.22E-16	1.52E-17	16051	7	5.75E-20	7.39E-22	297.0	10.7	378.6	8.4	18.5	0.4	107.5	30.7	0.7	0	0	na	0
Grain10	50	3.0	8	0.0234	1.8	1.05E-15	1.88E-17	18351	12	5.69E-20	7.65E-22	292.3	10.6	388.0	8.6	18.7	0.4	109.9	29.7	0.7	0	0	na	0
Grain11	50	1.3	6	0.0139	3.3	6.19E-16	2.05E-17	11486	4	5.39E-20	9.81E-22	302.2	10.9	377.6	8.4	18.3	0.4	107.0	28.9	0.8	0	0	na	0
Grain12	50	1.3	6	0.0087	4.4	3.90E-16	1.73E-17	6788	4	5.74E-20	1.21E-21	269.5	9.8	376.9	8.3	17.1	0.4	105.7	31.2	0.9	0	0	na	0
Grain13	50	1.3	6	0.0102	4.5	4.57E-16	2.08E-17	7473	8	6.12E-20	1.31E-21	293.8	10.6	384.5	8.5	19.9	0.4	110.3	31.8	0.9	0	0	na	0
Grain14	50	1.3	4	0.0069	4.6	3.08E-16	1.42E-17	5187	3	5.94E-20	1.27E-21	303.9	11.1	382.6	8.6	19.8	0.4	109.7	31.1	0.9	0	0	na	0
Grain15	50	1.3	2	0.0038	6.1	1.69E-16	1.04E-17	2763	2	6.12E-20	1.52E-21	295.9	10.8	385.3	8.5	19.9	0.4	110.4	31.8	1.0	0	0	na	0
Grain16	50	1.3	2	0.0034	8.6	1.52E-16	1.31E-17	2450	1	6.20E-20	1.82E-21	279.9	10.3	387.2	8.6	20.6	0.5	111.6	31.9	1.1	0	0	na	0
Grain17	50	1.3	2	0.0034	7.8	1.50E-16	1.18E-17	2699	6	5.55E-20	1.56E-21	290.3	10.8	362.8	8.2	19.9	0.5	105.2	30.3	1.0	0	0	na	0
Grain18	50	1.3	4	0.0076	3.6	3.41E-16	1.24E-17	5493	72	6.21E-20	1.44E-21	273.6	10.4	384.2	8.7	21.0	0.5	111.3	32.0	0.9	0	0	na	0
Grain19	50	1.3	4	0.0074	4.5	3.31E-16	1.48E-17	5211	104	6.35E-20	1.85E-21	298.3	11.0	393.5	8.8	20.4	0.5	112.8	32.3	1.1	0	0	na	0
Grain20	50	1.3	8	0.0120	3.4	5.35E-16	1.82E-17	9800	41	5.46E-20	1.03E-21	279.8	10.4	357.1	8.0	18.9	0.4	102.9	30.5	0.8	0	0	na	0
Grain21	50	1.3	8	0.0132	3.3	5.90E-16	1.94E-17	10502	31	5.62E-20	1.03E-21	289.1	10.6	381.8	8.5	18.3	0.4	108.1	29.9	0.8	0	0	na	0
Grain22	50	1.3	8	0.0130	2.3	5.80E-16	1.32E-17	10509	10	5.52E-20	8.34E-22	287.1	10.5	376.5	8.4	18.2	0.4	106.7	29.7	0.7	0	0	na	0
Grain23	50	1.3	8	0.0124	2.5	5.54E-16	1.40E-17	9690	11	5.71E-20	9.11E-22	258.7	9.5	379.3	8.5	16.1	0.4	105.2	31.2	0.8	0	0	na	0
Grain24	50	1.3	8	0.0125	3.1	5.60E-16	1.75E-17	9400	23	5.95E-20	1.06E-21	257.4	9.3	385.2	8.5	16.2	0.4	106.7	32.0	0.8	0	0	na	0
Grain25	50	1.5	8	0.0145	2.8	6.49E-16	1.82E-17	11111	22	5.84E-20	9.85E-22	298.1	10.6	391.0	8.6	18.6	0.4	110.5	30.3	0.8	0	0	na	0
Grain26	50	1.5	8	0.0142	3.4	6.33E-16	2.13E-17	10826	89	5.85E-20	1.18E-21	289.1	13.8	387.8	12.3	17.9	0.6	109.0	30.8	1.0	0	0	na	0
Grain27	50	1.5	8	0.0155	1.6	6.93E-16	1.08E-17	10633	76	6.52E-20	9.38E-22	254.3	10.1	428.3	10.8	17.1	0.4	117.7	31.8	0.9	0	0	na	0
Grain28	50	2.0	8	0.0190	2.0	8.47E-16	1.70E-17	14241	165	5.95E-20	1.09E-21	241.9	9.5	405.1	10.1	16.4	0.4	111.5	30.7	0.8	0	0	na	0
Grain29	50	2.0	8	0.0176	1.9	7.87E-16	1.48E-17	13803	15	5.70E-20	7.83E-22	231.9	8.4	369.4	8.1	17.4	0.4	104.3	31.4	0.7	0	0	na	0
Grain30	50	2.5	8	0.0206	1.5	9.21E-16	1.38E-17	16123	27	5.71E-20	7.07E-22	240.5	8.7	383.5	8.5	17.8	0.4	108.0	30.4	0.7	0	0	na	0
Grain31	50	2.5	8	0.0217	1.8	9.67E-16	1.77E-17	15995	68	6.05E-20	8.57E-22	292.4	10.4	398.5	8.8	20.1	0.4	113.7	30.5	0.7	0	0	na	0
Grain32	50	2.5	8	0.0277	1.1	1.24E-15	1.37E-17	16197	13	7.63E-20	8.07E-22	319.8	11.3	497.7	11.0	25.9	0.6	142.8	30.7	0.7	0	0	na	0
Grain33	50	2.0	8	0.0188	2.7	8.41E-16	2.26E-17	13666	55	6.15E-20	1.04E-21	282.2	10.0	391.3	8.6	20.5	0.5	112.5	31.4	0.8	0	0	na	0
Grain35	50	3.0	8	0.0255	1.6	1.14E-15	1.85E-17	18148	20	6.28E-20	8.04E-22	299.7	11.1	383.5	9.2	20.4	0.5	110.5	32.6	0.8	0	0	na	0
Grain36	50	3.0	8	0.0237	1.6	1.06E-15	1.67E-17	18514	57	5.71E-20	7.39E-22	261.8	9.3	376.3	8.2	16.6	0.4	105.1	31.2	0.7	0	0	na	0
Average										***5.91±0.44E-20***		***278±25***		***385±24***		***18.7±1.9***		***109±7***	***31.04±1.04***				
Durango2																								
Grain01	*50*	*2.0*	*8*	*0.0088*	*2.0*	*3.94E-16*	*7.68E-18*	*2123*	-	*3.03E-20*	*5.91E-22*	*363.9*	*55.2*	*367.8*	*2.1*	*12.42*	*0.17*	*98.9*	*17.5*	*0.4*	*5*	*0*	*na*	*0*
Grain02	50	2.0	8	0.0153	2.3	6.83E-16	1.54E-17	7359	-	5.25E-20	1.18E-21	353.5	54.4	315.8	2.9	13.09	0.10	87.3	34.5	0.8	0	0	na	0
Grain03	50	2.0	8	0.0152	2.1	6.78E-16	1.42E-17	9057	-	5.22E-20	1.09E-21	253.5	39.3	326.8	3.1	13.49	0.10	90.3	33.1	0.8	0	0	na	0
Grain04	50	2.0	8	0.0182	1.5	8.12E-16	1.18E-17	7065	-	6.25E-20	9.10E-22	271.8	42.8	381.3	3.7	15.04	0.12	104.6	34.3	0.6	0	0	na	0
Grain05	*50*	*2.0*	*8*	*0.0054*	*3.0*	*2.39E-16*	*7.18E-18*	*2109*	-	*1.84E-20*	*5.52E-22*	*202.4*	*32.1*	*322.6*	*3.2*	*13.89*	*0.11*	*89.7*	*11.8*	*0.4*	*5*	*0*	*na*	*0*
Grain06	50	2.0	8	0.0119	1.7	5.31E-16	9.29E-18	5577	-	4.09E-20	7.15E-22	260.4	41.7	265.6	2.8	10.81	0.09	73.2	32.0	0.6	0	0	na	0
Grain07	50	2.0	8	0.0128	2.2	5.73E-16	1.28E-17	7819	-	4.41E-20	9.85E-22	224.5	36.2	298.7	3.9	11.73	0.11	81.9	30.9	0.8	0	0	na	0
Grain08	50	2.0	8	0.0111	2.5	4.97E-16	1.22E-17	6531	-	3.83E-20	9.40E-22	192.1	31.2	270.3	2.9	11.06	0.09	74.6	29.4	0.8	0	0	na	0
Grain09	50	2.0	8	0.0124	2.8	5.55E-16	1.53E-17	6400	-	4.27E-20	1.18E-21	245.4	40.6	266.5	2.7	11.22	0.10	73.9	33.1	1.0	0	0	na	0
Grain10	50	2.0	8	0.0125	2.0	5.58E-16	1.11E-17	7398	-	4.29E-20	8.51E-22	277.2	46.2	265.8	2.7	11.35	0.10	73.8	33.3	0.7	0	0	na	0
Grain11	50	2.0	8	0.0125	1.9	5.60E-16	1.07E-17	7592	-	4.31E-20	8.20E-22	270.2	45.4	267.5	2.8	11.26	0.10	74.1	33.3	0.7	0	0	na	0
Grain12	50	2.0	8	0.0115	2.5	5.14E-16	1.29E-17	7427	-	3.95E-20	9.94E-22	277.9	47.1	249.8	2.6	11.75	0.11	70.4	32.1	0.8	0	0	na	0
Grain13	50	2.0	8	0.0137	1.7	6.14E-16	1.07E-17	7204	-	4.72E-20	8.21E-22	216.1	37.0	337.7	3.5	14.87	0.14	94.2	28.8	0.5	0	0	na	0
Grain14	50	2.0	8	0.0128	2.0	5.70E-16	1.11E-17	7905	-	4.39E-20	8.56E-22	221.5	38.2	324.3	3.4	15.30	0.14	91.5	27.5	0.6	0	0	na	0
Grain15	50	2.0	8	0.0153	2.1	6.81E-16	1.42E-17	7213	-	5.24E-20	1.09E-21	236.2	41.5	379.3	2.9	13.66	0.16	102.8	29.3	0.6	0	0	na	0
Grain16	50	2.0	8	0.0128	1.2	5.73E-16	6.89E-18	7320	-	4.41E-20	5.30E-22	220.4	39.1	270.7	2.9	12.67	0.12	76.27	33.2	0.5	0	0	na	0
Grain17	50	2.0	8	0.0129	1.8	5.77E-16	1.02E-17	7241	-	4.44E-20	7.85E-22	193.2	34.6	268.6	2.9	12.89	0.13	76.0	33.5	0.7	0	0	na	0
Grain18	50	2.0	8	0.0122	1.6	5.44E-16	8.90E-18	8182	-	4.18E-20	6.85E-22	203.4	36.8	278.3	1.7	12.56	0.14	78.0	30.8	0.6	0	0	na	0
Grain19	50	2.0	8	0.0145	1.7	6.47E-16	1.10E-17	7857	-	4.98E-20	8.44E-22	210.6	38.4	442.8	4.5	16.22	0.16	120.3	23.8	0.4	0	0	na	0
Grain20	50	2.0	8	0.0199	1.3	8.88E-16	1.19E-17	7768	-	6.83E-20	9.15E-22	207.4	38.6	439.3	4.3	15.55	0.16	118.8	33.0	0.5	0	0	na	0
Grain21	50	2.0	8	0.0127	1.9	5.65E-16	1.08E-17	7873	-	4.35E-20	8.31E-22	206.0	38.8	278.0	2.8	11.12	0.12	76.5	32.6	0.7	0	0	na	0
Grain22	*50*	*2.0*	*8*	*0.0126*	*2.3*	*5.64E-16*	*1.27E-17*	*10187*	-	*4.34E-20*	*9.78E-22*	*286.7*	*54.5*	*332.0*	*3.2*	*14.93*	*0.16*	*92.9*	*26.8*	*0.7*	*5*	*0*	*na*	*0*
Grain23	50	2.0	8	0.0175	1.3	7.80E-16	1.04E-17	8753	-	6.00E-20	7.98E-22	221.1	42.5	412.5	3.6	15.93	0.18	112.9	30.5	0.5	0	0	na	0
Grain24	50	2.0	8	0.0157	1.8	7.00E-16	1.23E-17	7825	-	5.38E-20	9.48E-22	209.6	40.7	374.2	1.7	13.98	0.07	101.9	30.3	0.5	0	0	na	0
Grain25	50	2.0	8	0.0163	1.1	7.26E-16	8.26E-18	8235	-	5.58E-20	6.36E-22	138.7	27.2	374.1	4.2	14.75	0.16	102.7	31.2	0.5	0	0	na	0
Average				***0.014±0.00323***		***6.28±1.04E-16***		***7527±757***		***4.83±0.80E-20***		***232±43***		***322±61***		***13.2±1.78***		***89±16***	***31.38±2.53***					
22BGE055T																								
Grain01	30	2.0	6	0.0050	3.9	2.25E-16	8.76E-18	3412		6.60E-20	2.57E-21	57.59	5.50	72.50	0.43	33.26	0.22	50.3	75.4	2.9	0	1	0	0
Grain02	30	2.0	6	0.0040	5.7	1.77E-16	1.01E-17	3578		4.94E-20	2.82E-21	79.46	7.67	26.00	0.15	41.42	0.27	47.5	59.7	3.4	0	0	3	0
Grain04	*30*	*2.0*	*6*	*0.0123*	*2.8*	*5.51E-16*	*1.53E-17*	*3489*		*1.58E-19*	*4.38E-21*	*92.90*	*9.05*	*30.27*	*0.17*	*83.81*	*0.55*	*90.9*	*99.4*	*2.7*	*0*	*0*	*5*	*0*
Grain05	30	2.0	6	0.0060	3.1	2.68E-16	8.19E-18	3568		7.51E-20	2.30E-21	15.23	1.51	25.61	0.14	47.86	0.32	53.9	79.8	2.5	0	1	2	0
Grain06	30	2.0	6	0.0050	3.8	2.24E-16	8.63E-18	3473		6.46E-20	2.48E-21	54.26	5.45	44.85	0.25	34.73	0.23	45.3	81.8	3.1	0	0	0	0
Grain07	30	2.0	6	0.0053	5.2	2.35E-16	1.23E-17	3658		6.42E-20	3.35E-21	0.00	85.34	141.22	1.22	50.76	0.44	83.9	36.2	10.0	0	4	0	2
Grain08	30	2.0	6	0.0109	2.4	4.87E-16	1.19E-17	3237		1.50E-19	3.67E-21	178.05	18.22	149.80	0.81	97.21	0.66	132.4	65.2	1.5	0	1	0	0
Grain09	30	2.0	6	0.0054	5.0	2.43E-16	1.21E-17	3314		7.34E-20	3.64E-21	49.14	5.08	50.65	0.27	47.14	0.32	59.0	71.4	3.6	0	0	3	1
Grain10	*30*	*2.0*	*6*	*0.0060*	*4.2*	*2.66E-16*	*1.10E-17*	*3538*		*7.52E-20*	*3.12E-21*	*32.02*	*3.34*	*11.23*	*0.06*	*55.26*	*0.38*	*57.9*	*74.6*	*3.1*	*0*	*0*	*5*	*0*
Grain11	30	2.0	6	0.0049	3.2	2.18E-16	6.91E-18	3372		6.46E-20	2.05E-21	30.50	3.24	44.09	0.23	31.11	0.21	41.5	89.2	2.9	0	0	2	2
Grain12	*30*	*2.0*	*6*	*0.0081*	*2.2*	*3.64E-16*	*8.14E-18*	*3349*		*1.09E-19*	*2.43E-21*	*256.59*	*27.53*	*136.38*	*0.71*	*122.95*	*0.87*	*155.0*	*40.2*	*1.0*	*0*	*5*	*0*	*0*
Grain13	30	2.0	6	0.0063	3.1	2.82E-16	8.69E-18	3417		8.25E-20	2.54E-21	166.27	18.01	97.89	0.49	49.59	0.34	72.6	65.1	2.1	0	1	0	0
Grain14	30	2.0	6	0.0043	3.0	1.93E-16	5.70E-18	3458		5.58E-20	1.65E-21	41.18	4.50	52.71	0.26	29.85	0.21	42.2	75.9	2.3	0	0	0	0
Grain15	30	2.0	6	0.0052	5.2	2.34E-16	1.21E-17	3503		6.68E-20	3.46E-21	24.05	2.65	38.12	0.18	34.65	0.24	43.6	87.8	4.5	0	0	0	0
Grain17	30	2.0	6	0.0070	2.3	3.10E-16	7.22E-18	3598		8.63E-20	2.01E-21	26.09	2.90	14.42	0.07	59.43	0.41	62.8	78.7	1.8	0	1	0	0
Grain18	30	2.0	6	0.0090	2.6	4.00E-16	1.04E-17	3377		1.18E-19	3.09E-21	119.91	13.59	45.82	0.20	65.95	0.46	76.7	88.5	2.4	0	0	0	0
Grain19	30	2.0	6	0.0154	1.6	6.88E-16	1.10E-17	3800		1.81E-19	2.89E-21	295.89	33.85	103.95	0.44	103.31	0.72	127.8	81.0	1.4	0	1	3	2
Grain20	30	2.0	6	0.0033	5.4	1.46E-16	7.88E-18	3593		4.05E-20	2.19E-21	46.81	5.40	12.81	0.05	60.48	0.42	63.5	36.7	1.9	0	0	3	0
Grain21	*30*	*2.0*	*6*	*0.0167*	*2.3*	*7.44E-16*	*1.73E-17*	*3987*		*1.87E-19*	*4.34E-21*	*163.43*	*19.03*	*47.84*	*0.21*	*88.52*	*0.64*	*99.8*	*106.8*	*2.5*	*0*	*5*	*3*	*0*
Grain22	*30*	*2.0*	*6*	*0.0063*	*2.8*	*2.81E-16*	*7.94E-18*	*3399*		*8.27E-20*	*2.33E-21*	*20.66*	*2.43*	*10.98*	*0.04*	*67.53*	*0.47*	*70.1*	*67.7*	*1.9*	*0*	*0*	*5*	*0*
Average				***0.0073±0.0037***		***3.27±1.67E-16***		***3506±172***		***9.25±4.36E-20***		***87.5±83.4***		***57.9±44.5***		***60.2±26.5***		***'3.8±32.6***	***71.48±21.48***					

All samples were measured with a laser repetition rate of 10 Hz

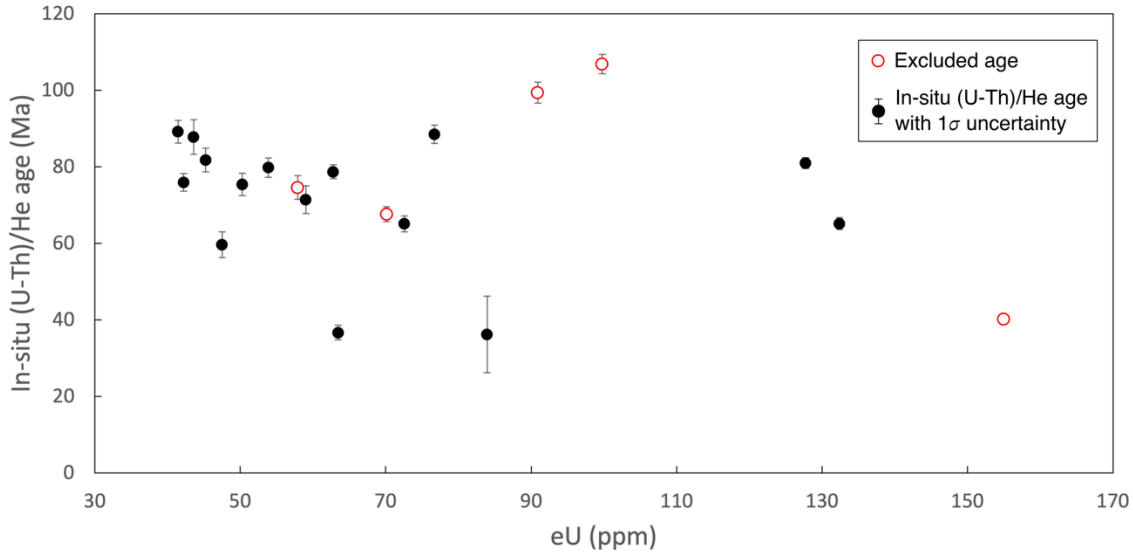

Figure 5: Relation between apatite in-situ (U-Th)/He ages (Ma) and eU (ppm) of sample 22BGE055T.

5 Discussion

This section addresses three key aspects relevant to the interpretation of the thermochronological data presented in this study. First, we evaluate the potential effects of the proposed sample mounting procedure on the (U-Th)/He and fission-track systems, specifically considering the possibility of helium diffusion and fission-track annealing. Second, we outline the criteria used to exclude individual apatite grains from interpretation in the in-situ (U-Th)/He analysis, focusing on petrographic and geochemical indicators of disturbed or unreliable data. Finally, we integrate the new thermochronological results obtained for sample 22BGE055T to interpret the thermal evolution of the Odenwald region, providing insights into its exhumation history and placing the findings in the context of existing regional studies.

5.1 He diffusion and fission track annealing during mounting

Each dating method applied in this study (fission track (FT), in situ (U-Th)/He, and U-Pb) requires specific sample preparation constraints to ensure analytical precision and reliability. For instance, fission tracks must be etched to become optically visible, necessitating chemically resistant embedding media. Traditionally, epoxy is used for apatite FT and U-Pb analysis, whereas thin Teflon films are preferred for zircon due to their resistance to etchants and optical transparency. In contrast, in situ (U-Th)/He dating requires sample mounts that are ultra-high vacuum (UHV) compatible, which excludes most conventional epoxies due to their relatively high vapor pressure. Additionally, for LA-ICP-MS analyses used in U-Pb dating and trace element measurements, a rigid and flat mount surface is essential. This ensures consistent laser focus and reproducible ablation pit geometry, which are critical for accurate dating and elemental quantification. As a result, epoxy mounts are commonly used in these applications.

Implementing double or triple dating on the same grains requires a methodological compromise, given the differing mounting requirements of each technique. Previous studies have proposed various solutions, such as re-mounting grains from epoxy into indium (e.g., Boyce et al., 2016), using Teflon-aluminium composite mounts (Pickering et al., 2020), or embedding directly in Teflon (e.g., Tripathy-Lang et al., 2013; Evans et al., 2015). However, each method has limitations. Re-mounting is labour-intensive and carries the risk of grain loss, while Teflon-aluminium composites are opaque, making them unsuitable for transmitted light microscopy necessary for FT counting.

The embedding method applied here using Teflon film requires heating grains to temperatures close to 300°C, clearly exceeding the temperature at which He diffusion and fission track annealing in apatite is significant over geological timescales (e.g. Ketcham et al. 1999; Farley 2000). We therefore evaluated the effect of the mounting using 1D thermal history modelling and comparing fission track length distributions of samples mounted with epoxy (without heating) and Teflon (with heating). The modelling indicates that brief heating (~1.5 minutes at 300 °C) does not affect apatite (U-Th)/He or fission track ages, and results in only minimal track length reduction. For previously unannealed fluorapatite grains, the model predicts a reduction of ~0.1 µm, which would be even smaller for more annealing-resistant tracks (e.g., pre-annealed or Cl-rich apatite). Consistent with this, measured mean track lengths (MTL) from fluorapatites in southwestern Germany with pre-annealed tracks show only a minor reduction within measurement uncertainty of 0.03 µm (13.12 µm in epoxy vs. 13.09 µm in Teflon mounts). Thus, embedding apatite in Teflon at 300 °C does not lead to significant He diffusion or FT annealing (Table 2). However, careful control of heating duration and temperature during mounting is essential.

5.2 Excluding individual spot analysis when applying the in-situ (U-Th)/He method

As detailed in Sect. 2, the in-situ (U-Th)/He dating protocol involves a series of preparation and analytical steps that can be lengthy and technically demanding. Consequently, not all grains subjected to this procedure will yield data suitable for interpretation. To maintain data quality and analytical consistency, it is essential to apply pre-defined exclusion criteria for the selection of acceptable grains. Based on our experience and previous studies, we propose a decision matrix that evaluates four key criteria: laser pit shape, radionuclide zoning, grain geometry, and the pit–grain relationship (Fig. 6).

Laser pit shape

The laser pit shape is influenced both by the laser beam properties and the physical condition of the grain surface. Ideally, the laser pit should be circular with steep, vertical walls and a flat base, characteristics that occur when the laser energy is evenly distributed, the focus is precise, and the grain surface is free of roughness, inclusions, or fractures (Fig. 6). Deviations from these ideal conditions, such as irregular pit outlines, sloping walls, or surface chipping, complicate accurate volume estimation and may lead to incomplete helium release during ablation (see supplement figure S3 for examples). The uncertainty of laser pit volume estimations will increase from grade 1 to 4, likely by a few percent, whereas pits that display significant edge overlap or evidence of chipped-off fragments should be excluded from interpretation.

Radionuclide zoning

In terms of radionuclide zoning, it is important to recognize that the measured helium originates from a surrounding diffusion domain approximately 40 μm in radius. However, due to the partial removal of this domain during grinding and polishing, only a fraction of the total helium-producing volume is retained in the final measurement. Consequently, even visually homogeneous grains may still be influenced by zoning within the original contributing volume. To evaluate the uniformity of the radionuclide distribution in the ablation zone, we propose the use of the mean square of weighted deviates (MSWD) determined for the depth-corrected radionuclide concentrations as a diagnostic metric. A value near 1 suggests a uniform distribution of parent nuclides, while elevated MSWD values indicate significant zoning or compositional heterogeneity. An MSWD value of 5 or 10 roughly corresponds to a core-to-rim ratio of radionuclides of 1.5 and 2 and would result in whole-grain apatite (U-Th)/He age variation of roughly 5 and 10% (e.g. Glotzbach and Ehlers 2024). Grains with pronounced zoning and MSWD values exceeding 20 result in age deviations >10%, and should be, together with grains with visible inclusions, excluded to ensure reliable interpretation.

Grain geometry

The geometry of the mineral grain is another critical factor affecting the interpretation of in-situ (U-Th)/He analyses. Since alpha particles have long alpha stopping distances (up to 40 μm), grain shape influences both helium production and retention. Ideally, analyses should target euhedral grains with well-preserved, flat prismatic surfaces. Complex or irregular morphologies introduce uncertainties in modeling alpha-ejection and diffusion pathways. Exceptions can be made for large shards (e.g., Durango apatite), where geometric uncertainties have a negligible impact on resulting ages. The grain geometry therefore does not necessarily impact the resulting ages but is an important constraint for thermal history modelling. Measuring the grain diameter and reporting the grain length are essential for thermal history modelling. In cases where the tips of long-prismatic crystals are broken, reliable modelling remains feasible if the preserved prism length is at least twice the grain diameter.

Pit-grain relationship

The spatial relationship between the laser-ablation pit and the mineral grain must be carefully considered due to the relatively long alpha-stopping distances. Of primary importance is the distance from the pit to the nearest prismatic face and the grain tip. These distances must be well constrained and visually verifiable. Ideally, the pit should be located near the center of the grain to minimize edge effects and ensure a well-constrained alpha-ejection correction. Slight deviations toward the prismatic face or grain tip are acceptable, provided the pit remains fully within the grain and avoids complex or irregular edges. Conversely, intentionally placing several pits within the same grain, while some are placed closer to the prismatic face, enables reconstruction of the thermal history of a single grain (Glotzbach and Ehlers, 2024; Maier et al. 2026). Measurements where the pit is too close to highly curved or irregular boundaries introduce geometric uncertainties and should be treated with caution. In particular, pits that are partly outside the grain must be excluded, as they compromise both the helium yield and the alpha-ejection correction, leading to unreliable age estimates.

	Laser pit shape	Radio-nuclide zoning	Grain geometry	Pit-grain relationship
1 - perfect	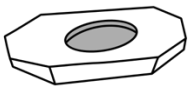 round, vertical walls, flat bottom	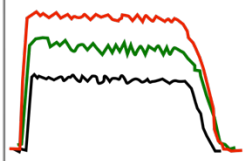 uniform, MSWD ~1	 euhedral grain with minimal surface curvature	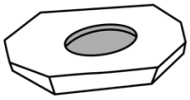 pit centered, far from edges
2	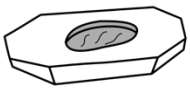 slightly irregular shape or depth	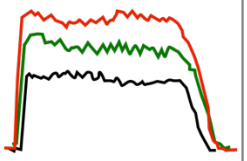 slight variations, MSWD >1	 slightly deformed euhedral grain	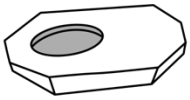 pit not centered, but >40 µm away from edges
3	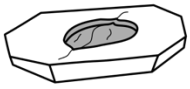 rough surfaces or broken edges	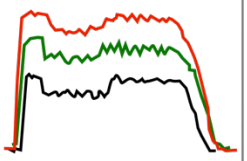 moderate zoning, MSWD >5	 partly broken euhedral grain	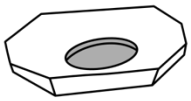 pit not centered, and <40 µm away from edges
4	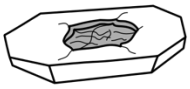 strong surface roughness	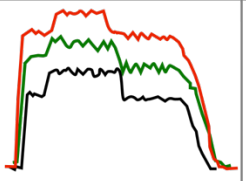 strong zoning, MSWD>10	 euhedral grain with tips broken off, subhedral grain	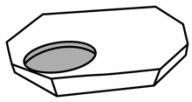 pit not centered, and <40 µm away from edges
5 - excluded	 chipped off or incomplete	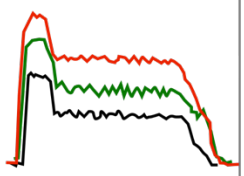 extreme zoning, MSWD>20	 subhedral grain, without clear grain bounaries	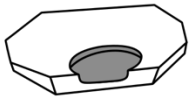 pit crosses grain edge

659

Figure 6: Decision matrix to rank/exclude in-situ (U-Th)/He measurements. The red, green and black lines in the second column (Radionuclide zoning) represent counts measured by LA-ICP-MS for trace elements such as radionuclides (U, Th, Sm).

5.2 Tradeoffs and limitations of the triple dating approach

The benefits of combining multiple thermochronological and geochronological methods on a single apatite grain have been extensively demonstrated, including improved interpretation of grain-specific thermal histories, direct comparison of chronometers, and reduction of uncertainties associated with inter-grain variability (e.g., Boyce et al., 2006; Glotzbach and Ehlers, 2024; Maier et al., 2026). Nevertheless, the triple-dating approach combining in-situ (U-Th)/He, fission track, and U-Pb analyses also involves several methodological compromises that should be carefully considered.

A principal limitation arises from the in-situ (U-Th)/He analyses, which are performed on polished internal grain surface. Consequently, approximately half of the grain volume is inaccessible for analysis. Because the measured parent nuclide concentrations are only representative of the exposed section, variations in U and Th concentrations perpendicular to the polished surface cannot be directly assessed. Such depth-dependent zoning may significantly influence calculated (U-Th)/He ages but would be impossible to quantify parts of the grain that are ground and polished away. We therefore strongly recommend evaluating radionuclide zoning from the remaining grain and excluding grains that exhibit pronounced chemical heterogeneity. Future work should focus on systematically characterizing three-dimensional radionuclide distributions in apatite, quantifying their influence on in-situ (U-Th)/He ages, and establishing practical criteria for identifying and treating problematic grains. In this study, we propose the mean square of weighted deviates (MSWD) of parent nuclide concentrations as a first-order indicator of chemical heterogeneity. However, this metric should be regarded only as a rough proxy because it does not account for the spatial distribution of the zoning within a grain. For example, parent nuclide enrichment near the grain rim is expected to have a different effect on the calculated (U-Th)/He age than comparable heterogeneity concentrated in the grain interior (e.g., Glotzbach and Ehlers, 2024). More sophisticated approaches that explicitly incorporate the geometry of radionuclide zoning are therefore desirable.

The integration of fission track analysis within the triple-dating workflow also requires methodological compromises. In conventional apatite fission track dating using the external detector method, spontaneous tracks can be counted over irregularly shaped polished surfaces, maximizing the available counting area. In contrast, the LA-ICP-MS approach requires the counting area to coincide with the laser ablation geometry, which is typically circular or square and of similar size for all grains. This restriction generally reduces the number of spontaneous tracks available for counting and therefore decreases the precision of individual fission track ages. To partially compensate for this limitation, we routinely count and measure multiple areas within a single grain, provided the grain size permits, thereby increasing the total spontaneous track count and improving the robustness of the fission track data.

A further consideration is the simultaneous acquisition of rare earth element (REE) and U-Pb data. In principle, collecting both datasets within the same analytical session could reduce the spatial resolution of radionuclide

imaging with depth if additional dwell time were required for the REE measurements. However, our analytical protocol minimizes this effect by employing element-specific integration times. Rare earth elements are measured with an integration time of 0.001 s per mass, whereas U, Th, and Pb isotopes are measured with an integration time of 0.1 s per mass. Given that the total integration time for a complete measurement cycle is approximately 1 s, the cumulative REE acquisition time of only 0.014 s is negligible and does not measurably reduce the spatial resolution of the U-Th-Pb dataset.

Overall, while the triple-dating approach requires several analytical compromises, these limitations are outweighed by the unique ability to directly integrate U-Pb crystallization ages, REE patterns, fission track cooling ages, and (U-Th)/He thermochronology from the same apatite grain. Awareness of the inherent tradeoffs and careful screening of grains for chemical heterogeneity are essential to ensure robust interpretation of the resulting datasets.

5.3 Thermal history application

To reconstruct the thermal evolution of the crystalline basement in the Odenwald region, we performed inverse thermal history modelling of sample 22BGE055T. This sample was collected from exposed granodioritic basement and represents a key location for understanding the post-Variscan to Cenozoic cooling and exhumation history of the Odenwald. The modelling approach combines apatite fission track (AFT) data and in-situ (U-Th)/He thermochronometry, utilizing the annealing model of Ketcham et al. (2007) for fission tracks and the diffusion model of Flowers et al. (2009), adapted for in-situ measurements following Glotzbach and Ehlers (2024). Thermal history modelling was implemented in MATLAB using an inverse modelling approach similar to that employed by the HeFTy software. Candidate time–temperature (t–T) paths were generated through a random search and evaluated against available thermochronological data. Independent geological constraints, including the U–Pb crystallization age of the sample and stratigraphic constraints on the post-emplacement burial history, were imposed to restrict the range of thermal histories. Because forward modelling of 15 individual in-situ (U-Th)/He ages is computationally demanding, whereas AFT annealing calculations are comparatively fast, the modelling was performed in two stages. First, 300 random t–T paths that provided acceptable fits to the AFT data were identified. These AFT-compatible thermal histories were subsequently used as input for forward modelling of the individual AHe ages, substantially reducing the computational effort while ensuring consistency with the AFT constraints. Analogous to the HeFTy thermal history modelling software, the goodness of fit (GOF) statistic was used to quantify the agreement between the predicted and observed thermochronological data and to assess the acceptability of each thermal history.

The input dataset includes a central AFT age of 92.1 ± 5.8 Ma, a measured track length distribution with a mean track length (MTL) of 12.61 ± 1.20 μm, a Dpar of 1.59 μm, and a set of 15 single-grain in-situ He measurements, each accompanied by detailed radionuclide concentrations and grain-specific geometries (see Table 5). Modelling requires determining the pit radius, pit depth, grain radius and the closest distance between the laser pit and the prismatic face. The latter was measured on the polished surface (Dist2PrismX), and in the vertical direction by focusing on the bottom of the grain with transmitted light using a 100x objective (Dist2PrismZ). The smaller of the two measurements was used for modelling. To avoid unrealistic thermal histories, we applied three independent geological time-temperature

(tT) constraints. The first is based on the concordant apatite U-Pb age of 298.5 ± 7.2 Ma (Fig. 4D), corresponding to temperatures between 370 and 500°C (Mezger et al., 1989), indicative of late-stage cooling after pluton emplacement. The second constraint corresponds to early Triassic time (247.5–252.5 Ma). The 22BGE055T sample was collected a few hundred meters below the unconformity between the crystalline basement and the overlying early-Triassic clastic sedimentary rocks of the Buntsandstein, suggesting the temperature was likely 20-50°C at that time. The third constraint is the present-day surface temperature, fixed at 10°C.

Table 5: In-situ apatite (U-Th)/He data input for thermal history modelling of sample 22BGE055T.

Sample	He (at/g)	He 1σ (at/g)	U (ppm)	U 1σ (ppm)	Th (ppm)	Th 1σ (ppm)	Sm (ppm)	Sm 1σ (ppm)	Dist2PrismX (µm)	Dist2PrismZ (µm)	Grain Radius (µm)	Pit Radius (µm)	Pit Depth (µm)
Grain01	1.24E+16	4.83E+14	33.3	0.2	72.5	0.4	57.6	5.5	91	94	128	15	7
Grain02	9.29E+15	5.31E+14	41.4	0.3	26.0	0.1	79.5	7.7	120	112	131	15	7
Grain05	1.41E+16	4.32E+14	47.9	0.3	25.6	0.1	15.2	1.5	49	57	58	15	7
Grain06	1.22E+16	4.68E+14	34.7	0.2	44.9	0.2	54.3	5.4	76	77	104	15	7
Grain07	1.21E+16	6.31E+14	50.8	0.4	141.2	1.2	0.0	0.0	28	26	32	15	7
Grain08	2.83E+16	6.91E+14	97.2	0.7	149.8	0.8	178.1	18.2	57	75	97	15	7
Grain09	1.38E+16	6.85E+14	47.1	0.3	50.7	0.3	49.1	5.1	35	61	85	15	7
Grain11	1.22E+16	3.86E+14	31.1	0.2	44.1	0.2	30.5	3.2	29	45	38	15	7
Grain13	1.55E+16	4.79E+14	49.6	0.3	97.9	0.5	166.3	18.0	51	53	62	15	7
Grain14	1.05E+16	3.10E+14	29.9	0.2	52.7	0.3	41.2	4.5	50	141	101	15	7
Grain15	1.26E+16	6.52E+14	34.7	0.2	38.1	0.2	24.1	2.7	68	141	101	15	7
Grain17	1.62E+16	3.77E+14	59.4	0.4	14.4	0.1	26.1	2.9	66	55	70	15	7
Grain18	2.23E+16	5.81E+14	66.0	0.5	45.8	0.2	119.9	13.6	53	55	67	15	7
Grain19	3.40E+16	5.45E+14	103.3	0.7	103.9	0.4	295.9	33.8	27	65	67	15	7
Grain20	7.62E+15	4.13E+14	60.5	0.4	12.8	0.1	46.8	5.4	101	62	103	15	7

Dist2PrismX is the distance of the center of the laser pit towards the closest prism grain edge within the polished section. Dist2PrismZ is the distance of the polished section towards the grain bottom.

Given the large and complex dataset, we split the inverse modelling process into two stages to improve computational efficiency. In the first step, we generated one million random time-temperature paths and evaluated their fit against the fission track age and length distribution. Paths that yielded acceptable or good goodness-of-fit (GOF) values, as defined by Ketcham (2005), were retained. In the second step, 300 of these acceptable paths were randomly selected and evaluated against the in-situ (U-Th)/He data. Models were ranked according to how many input datasets they could reproduce with a GOF > 0.05 (Fig. 7). Although no single model fit all datasets simultaneously, the best-performing model successfully fit nine datasets: the fission track age, the track length distribution, and seven of the in-situ He concentrations (Fig. 8).

The ensemble of successful models reveals a well-defined thermal history, especially after ~150 Ma. Earlier stages are more loosely constrained and rely primarily on the imposed geological tT constraints. Following the emplacement of the granodiorite at ca. 320–330 Ma (Kreuzer and Harre, 1975) and depths of ~15 km (Stein and Dietl, 2001), rapid post-intrusion cooling is supported by the apatite U-Pb age of ~300 Ma. Stratigraphic and thermochronologic evidence suggests that the crystalline basement was largely exhumed by the end of the Permian, followed by a prolonged phase of reheating due to continued sedimentation and burial, likely persisting until the Late Jurassic. The modelled thermal peak exceeded 90°C, sufficient to fully reset both the AFT and AHe systems.

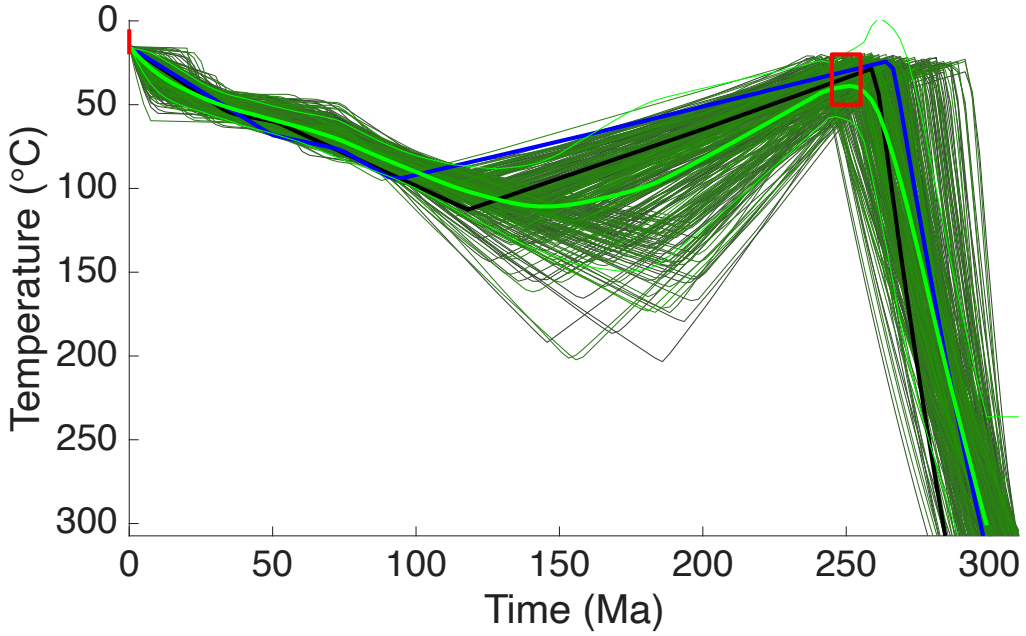

Figure 7: Modelled tT-path of sample 22BGE055T using apatite fission track and in-situ (U-Th)/He data. Paths are color-ranked according to their fit from black to light green with the thick green line is the weighted mean cooling paths with 95% CI (thin green lines). The tT-path that fit best the data is shown in blue (highest summed GOF) and black (most input data fitted with GOF>0.05). The red box is constraining the cooling paths to represent late Permian exhumation to near surface temperatures.

The thermochronological data do not precisely resolve the timing of basin inversion, but according to the reconstructed cooling paths it must have occurred before ~90 Ma (Fig. 7). Nevertheless, the modelling identifies two distinct cooling episodes that correlate well with known geodynamic events in the region. The first, during the Late Cretaceous, likely reflects regional doming and erosion, consistent with evidence of contemporaneous volcanism (Binder et al., 2023). The second major cooling phase, occurring after ~40 Ma, aligns with the initial development of the Upper Rhine Graben and the associated uplift of the graben shoulders, including the Odenwald. Since its emplacement, the Katzenbuckel volcano has beed eroded down to the Buntsandstein, indicating approximately 600 meters of post-69 Ma erosion (e.g. Wagner 1969), consistent with the amount of exhumation required to produce the cooling observed in sample 22BGE055T.

In summary, combined thermal history modelling using AFT and apatite in situ (U-Th)/He data can be performed in a manner similar to modelling with AFT and whole-grain (U-Th)/He data. However, when large volumes of in-situ (U-Th)/He data are included, modeling becomes computationally intensive and may significantly slow down. Running the thermal modeling sequentially, as done in this study, rather than simultaneously, offers a practical approach to improve computational efficiency. The inverse thermal modeling of AFT and in-situ (U-Th)/He data for sample 22BGE055T reveals a complex thermal evolution, characterized by post-intrusive cooling, burial and reheating during the Mesozoic, and two distinct Cenozoic cooling phases associated with regional tectonic events.

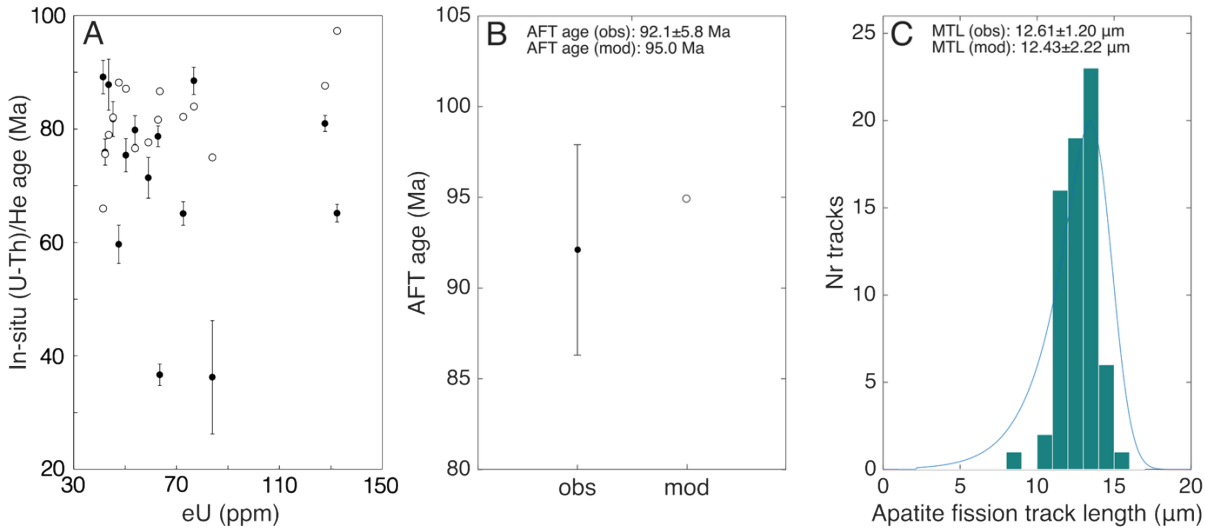

Fig. 8: Observed (obs) vs. modelled (mod) thermochronological data (black dots vs. circles) of sample 22BGE055T and the best fit tT-path that fit most input data simultaneously (black tT-path in Fig. 7).

6 Conclusion and broader applicability

This study introduces a practical and effective analytical method for triple-dating apatite grains using a Teflon-based mounting approach. The method facilitates the integration of AFT, in-situ (U-Th)/He, and U-Pb dating on the same grains, while preserving zoning information and geochemical context. Results presented here from the Durango apatite standard validate the technique's accuracy, and the application to a sample from crystalline rocks in the Odenwald reveals a detailed thermal history in line with major geodynamic episodes of the region. Importantly, we find that neither the fission track system nor helium diffusion are measurably affected during mount preparation. To improve the consistency and reliability of in-situ He data, we propose a decision matrix that aids in evaluating grain suitability based on critical geometric and analytical parameters.

The integrated approach presented here opens new possibilities for extracting multi-system geochronological and thermochronological information from single grains, particularly in complex tectonic settings. The relatively rapid sample procedure presented (compared to other protocols) avoids the time-consuming steps of extracting grains and/or remounting them for analysis by different techniques. More rapid sample processing also reduces analytical and labor costs. The procedures presented here enable higher throughput of individual grain analyses per sample. A higher throughput means that detrital samples (e.g., from river sediments, or sedimentary basins) can more easily be characterised for sediment provenance (e.g., Pujols and Stockli, 2021), catchment erosion patterns in locations with heterogeneous bedrock (e.g., Stock et al., 2006; Ehlers et al., 2015; Madella et al., 2022; Lukens et al., 2023) or hinterland exhumation or basin burial. Characterisation of sediment provenance is also enhanced by measurement of rare earth element variations between grains. Lastly, samples collected from bedrock benefit from this approach via

enhanced characterization of inter-grain variability in ages which can lead to better-resolved cooling histories and geologic interpretations.

Code availability

All mentioned scrips and apps together with user manuals describing in detail their usage are available from the associated Zenodo repository (https://doi.org/10.5281/zenodo.18979745).

Author contributions

Conceptualisation: TAE, CG. Formal analysis: CG, AN. Coding: CG. Visualization: CG. Writing: CG, AN, TAE.

Competing interests

The contact author has declared that none of the authors have any competing interests.

Acknowledgements

The paper improved through the thoughtful reviews of David Chew and Rebecca Flowers. Klaus Mezger and Stewart Fallon are thanked for editorial handling and technical corrections.

Financial support

This study was supported by the Bundesgesellschaft für Endlagerung (BGE – STAFuE-21-12-Klei) to Todd Ehlers and Christoph Glotzbach, and funding for large equipment from the Deutsche Forschungsgemeinschaft (DFG) to Todd Ehlers (INST 37/1041-1 FUGG, INST 37/1207-1 FUGG).

References:

Abdullin, F., Solari, L. A., Solé, J., & Ortega-Obregón, C.:Technical note: LA–ICP-MS U–Pb dating of unetched and etched apatites, Geochronology, 3(1), 59–65, https://doi.org/105194/gchron-3-59-2021, 2021.

Bedoya, A., Glorie, S., Hand, M., Kirkland, C. L., Kelsey, D. E., Nixon, A., & Fraser, G.: Apatite Triple Dating (Lu–Hf, U–Pb, FT) Constrains Deformation and Cooling in the Coompana and Madura Provinces, Western Australia, Lithosphere, 2023(Special 14), https://doi.org/10.2113/2023/lithosphere_2023_292, 2024.

Binder, T., Marks, M. A. W., Gerdes, A., Walter, B. F., Grimmer, J., Beranoaguirre, A., Wenzel, T., Markl, G.: Two distinct age groups of melilitites, foidites, and basanites from the southern Central European Volcanic Province reflect lithospheric heterogeneity, International Journal of Earth Sciences, 112(3), 881–905, https://doi.org/10.1007/s00531-022-02278-y, 2023.

Boyce, J. W., Hodges, K. V., Olszewski, W. J., Jercinovic, M. J., Carpenter, B. D., & Reiners, P. W.: Laser microprobe (U–Th)/He geochronology, Geochimica et Cosmochimica Acta, 70(12), 3031–3039, https://doi.org/10.1016/j.gca.2006.03.019, 2006.

Carrapa, B., DeCelles, P. G., Reiners, P. W., Gehrels, G. E., & Sudo, M.: Apatite triple dating and white mica 40Ar/39Ar thermochronology of syntectonic detritus in the Central Andes: A multiphase tectonothermal history, Geology, 37(5), 407–410, https://doi.org/10.1130/G25698A.1, 2009.

Chew, D. M., Donelick, R. A., Donelick, M. B., Kamber, B. S., & Stock, M. J.: Apatite Chlorine Concentration Measurements byLA-ICP-MS, Geostandards and Geoanalytical Research, 38(1), 23–35, https://doi.org/10.1111/j.1751-908x.2013.00246.x, 2014.

Cogné, N., Chew, D. M., Donelick, R. A., & Ansberque, C.: LA-ICP-MS apatite fission track dating: A practical zeta-based approach, Chemical Geology, 531, 119302, https://doi.org/10.1016/j.chemgeo.2019.119302, 2020.

Danišík, M., Shane, P., Schmitt, A. K., Hogg, A., Santos, G. M., Storm, S., Evans, N. J., Fifield, L. K., Lindsay, J. M.: Re-anchoring the late Pleistocene tephrochronology of New Zealand based on concordant radiocarbon ages and combined 238U/230Th disequilibrium and (U–Th)/He zircon ages, Earth and Planetary Science Letters, 349–350, 240–250, https://doi.org/10.1016/j.epsl.2012.06.041, 2012.

Donelick, R. A., O'Sullivan, P. B., & Ketcham, R. A.: Apatite Fission-Track Analysis, Reviews in Mineralogy and Geochemistry, 58(1), 49–94, https://doi.org/10.2138/rmg.2005.58.3, 2005.

Ehlers, T. A., Szameitat, A., Enkelmann, E., Yanites, B. J., & Woodsworth, G. J.: Identifying spatial variations in glacial catchment erosion with detrital thermochronology, Journal of Geophysical Research: Earth Surface, 120(6), 1023–1039, https://doi.org/10.1002/2014JF003432, 2015.

Evans, N. J., McInnes, B. I. A., McDonald, B., Danišík, M., Becker, T., Vermeesch, P., Shelley, M., Marillo-Sialer, E., Patterson, D. B.: An in situ technique for (U–Th–Sm)/He and U–Pb double dating, J. Anal. At. Spectrom., 30(7), 1636–1645, https://doi.org/10.1039/C5JA00085H, 2015.

Farley, K. A.: Helium diffusion from apatite: General behavior as illustrated by Durango fluorapatite, Journal of Geophysical Research: Solid Earth, 105(B2), 2903–2914, https://doi.org/10.1029/1999jb900348, 2000.

Glotzbach, C., & Ehlers, T. A.: Interpreting cooling dates and histories from laser ablation in situ (U–Th–Sm)/He thermochronometry: a modelling perspective, Geochronology, 6(4), 697–717, https://doi.org/10.5194/gchron-6-697-2024, 2024.

Flowers, R. M., Zeitler, P. K., Danišík, M., Reiners, P. W., Gautheron, C., Ketcham, R. A., Metcalf, J. R., Stockli, D. F., Enkelmann, E., Brown, R. W.: (U-Th)/He chronology: Part 1. Data, uncertainty, and reporting, GSA Bulletin, 135(1–2), 104–136, https://doi.org/10.1130/B36266.1, 2023.

Hasebe, N., Barbarand, J., Jarvis, K., Carter, A., & Hurford, A. J.: Apatite fission-track chronometry using laser ablation ICP-MS, Chemical Geology, 207(3–4), 135–145, https://doi.org/10.1016/j.chemgeo.2004.01.007, 2004.

Holder, R. M., Yakymchuk, C., & Viete, D. R.: Accessory Mineral Eu Anomalies in Suprasolidus Rocks: Beyond Feldspar, Geochemistry, Geophysics, Geosystems, 21(8), e2020GC009052, https://doi.org/10.1029/2020GC009052, 2020.

Horne, A. M., van Soest, M. C., Hodges, K. V., Tripathy-Lang, A., & Hourigan, J. K.: Integrated single crystal laser ablation U/Pb and (U–Th)/He dating of detrital accessory minerals – Proof-of-concept studies of titanites and zircons from the Fish Canyon tuff, Geochimica et Cosmochimica Acta, 178, 106–123, https://doi.org/10.1016/j.gca.2015.11.044, 2016.

Horne, A. M., van Soest, M. C., & Hodges, K. V.: U/Pb and (U-Th)/He "double" dating of detrital apatite by laser ablation: A critical evaluation, Chemical Geology, 506, 40–50, https://doi.org/10.1016/j.chemgeo.2018.12.004, 2019.

Iwano, H., Danhara, T., Danhara, Y., Hirabayashi, S., Nakajima, T., Sakai, H., & Hirata, T.: Zircon fission-track and U–Pb double dating using femtosecond laser ablation–inductively coupled plasma–mass spectrometry: A technical note, Island Arc, 29(1), https://doi.org/10.1111/iar.12348, 2020.

Jochum, K. P., Weis, U., Stoll, B., Kuzmin, D., Yang, Q., Raczek, I., Jacob, D. E., Stracke, A., Birbaum, K., Frick, D. A., Günther, D., Enzweiler, J.: Determination of Reference Values for NIST SRM 610–617 Glasses Following ISO Guidelines, Geostandards and Geoanalytical Research, 35(4), 397–429, https://doi.org/10.1111/j.1751-908x.2011.00120.x, 2011.

Ketcham, R. A., Donelick, R. A., & Carlson, W. D.: Variability of apatite fission-track annealing kinetics: III. Extrapolation to geological time scales, American Mineralogist, 84(9), 1235–1255, https://doi.org/10.2138/am-1999-0903, 1999.

Ketcham, R. A.: Forward and Inverse Modeling of Low-Temperature Thermochronometry Data, Reviews in Mineralogy and Geochemistry, 58(1), 275–314, https://doi.org/10.2138/rmg.2005.58.11, 2005.

Ketcham, R. A., Carter, A., Donelick, R. A., Barbarand, J., & Hurford, A. J.: Improved modeling of fission-track annealing in apatite, American Mineralogist, 92(5–6), 799–810, https://doi.org/10.2138/am.2007.2281, 2007.

Kreuzer, H., & Harre, W.: K/Ar-Altersbestimmung an Hornblenden und Biotiten des Kristallinen Odenwaldes, Aufschluss, 27, 71-77, 1975.

Larsen, R. B.: The distribution of rate-earth elements in K-feldspar as an indicator of petrogenetic processes in granitic pegmatites: examples from two pegmatite fields in southern Norway, The Canadian Mineralogist, 40, 137-151, 2002.

Longerich, H. P., Jackson, S. E., & Gunther, D.: Laser ablation inductively coupled plasma mass spectrometric transient signal data acquistion and analyte concentration calculation, Journal of Analytical Atomic Spectrometry, 11, 899-904, https://doi.org/10.1039/JA9961100899, 1996.

Lukens, C. E., Riebe, C. S., Sklar, L. S., & Shuster, D. L.: Sand, gravel, cobbles, and boulders: Detrital thermochronology shows that one size does not tell all. Journal of Geophysical Research: Earth Surface, 128, e2023JF007192. https://doi.org/10.1029/2023JF007192, 2023.

Madella, A., Glotzbach, C., & Ehlers, T. A.: How many grains are needed for quantifying catchment erosion from tracer thermochronology? Geochronology, 4(1), 177–190, https://doi.org/10.5194/gchron-4-177-2022, 2022.

Maier, A.-K., Glotzbach, C., & Falkowski, S.: Analytical and modelling strategies for thermal histories from in situ (U-Th-Sm)/He data of single apatites. Geochronology, 8, https://doi.org/10.5194/gchron-8-165-2026, 2026.

Mezger, K., Hanson, G. N., & Bohlen, S. R.: High-precision UPb ages of metamorphic rutile: application to the cooling history of high-grade terranes, Earth and Planetary Science Letters, 96(1–2), 106–118, https://doi.org/10.1016/0012-821x(89)90126-x, 1989.

McDowell, F. W., McIntosh, W. C., & Farley, K. A.: A precise 40Ar–39Ar reference age for the Durango apatite (U–Th)/He and fission-track dating standard, Chemical Geology, 214(3–4), 249–263, https://doi.org/10.1016/j.chemgeo.2004.10.002, 2005.

Paton, C., Woodhead, J. D., Hellstrom, J. C., Hergt, J. M., Greig, A., & Maas, R.: Improved laser ablation U-Pb zircon geochronology through robust downhole fractionation correction, Geochemistry, Geophysics, Geosystems, 11(3), 2009GC002618, https://doi.org/10.1029/2009GC002618, 2010.

Paul, A. N., Spikings, R. A., Chew, D. & Daly, J. S.: The effect of intro-crystal uranium zonation on apatite U-Pb thermochronology: A combined ID-TIMS and LA-MC-ICP-MS study, Geochimica et Cosmochimica Acta, 251, 15-35, https://doi.org/10.1016/j.gca.2019.02.013, 2019.

Paul, A. N., Spikings, R. A., & Gaynor, S. P.: U-Pb ID-TIMS reference ages and initial Pb isotope compositions for Durango and Wilberforce apatites, Chemical Geology, 586, 120604, https://doi.org/10.1016/j.chemgeo.2021.120604, 2021.

Pickering, J., Matthews, W., Enkelmann, E., Guest, B., Sykes, C., & Koblinger, B. M.: Laser ablation (U-Th)/He dating of detrital apatite, Chemical Geology, 548, 119683, https://doi.org/10.1016/j.chemgeo.2020.119683, 2020.

Pujols, E. J., % Stockli, D. F.: Zircon (U-Th)/(He-Pb) double-dating constraints on the interplay between thrust deformation and foreland basin architecture, Sevier foreland basin, Utah, Geosphere, 17(6), 1890-1913, https://doi.org/10.1130/GES02372.1, 2021.

Reiners, P. W., Campbell, I. H., Nicolescu, S., Allen, C. M., Hourigan, J. K., Garver, J. I., Mattinson, J. M., Cowan, D. S.: (U-Th)/(He-Pb) double dating of detrital zircons, American Journal of Science, 305(4), 259–311, https://doi.org/10.2475/ajs.305.4.259, 2005.

Schmitt, A. K, Marks, M., Nebor, A. W., & Markl, G.: The onset and origin of differential Rhine Graben volcanism based on U-Pb ages and oxygen isotopic composition of zircon, European Journal of Mineralogy, 19(6), 849-857, DOI: 10.1127/0935-1221/2007/0019-1776, 2007.

Stacey, J. S., & Kramers, J. D.: Approximation of terrestrial lead isotope evolution by a two-stage model, Earth and Planetary Science Letters, 26, 207-221, 1975.

Stein, E., & Dietl, C.: Hornblende thermobarometry of granitoids from the Central Odenwald (Germany) and their implications for the geotectonic development of the Odenwald, Mineralogy and Petrology, 72, 185-207, 2001.

Stock, G. M., Ehlers, T. A., & Farley, K. A.: Where does sediment come from? Quantifying catchment erosion with detrital apatite (U-Th)/He thermochronometry, Geology, 34(9), 725–728, https://doi.org/10.1130/G22592.1, 2006.

Tripathy-Lang, A., Hodges, K. V., Monteleone, B. D., & van Soest, M. C.: Laser (U-Th)/He thermochronology of detrital zircons as a tool for studying surface processes in modern catchments, Journal of Geophysical Research: Earth Surface, 118(3), 1333–1341, https://doi.org/10.1002/jgrf.20091, 2013.

Wagner, G. A.: Spuren der spontanen Kernspaltung des ^{238}Urans als Mittel der Datierung von Apatiten und ein Beitrag zur Geochronologie des Odenwaldes, N. Jb. Miner. Abh., 110(3), 252-286, 1969.

Will, T. M., Schmädicke, E., Ling, X.-X., Li, X.-H., & Li, Q.-L.: Geochronology, geochemistry and tectonic implications of Variscan granitic and dioritic rocks from the Odenwald-Spessart basement, Germany, Lithos, 404–405, 106454, https://doi.org/10.1016/j.lithos.2021.106454, 2021.

Williams, I. S.: U–Th–Pb geochronology by ion microprobe. In: McKibben, M.A., Shanks III, W.C., Ridley, W.I. (Eds.), Applications of microanalytical techniques to understanding mineralizing processes, Reviews in Economic Geology, 7, 1–35, 1998.

Zattin, M., Andreucci, B., Thomson, S. N., Reiners, P. W., & Talarico, F. M.: New constraints on the provenance of the ANDRILL AND-2A succession (western Ross Sea, Antarctica) from apatite triple dating: APATITE TRIPLE DATING IN ANTARCTICA, Geochemistry, Geophysics, Geosystems, 13(10), https://doi.org/10.1029/2012GC004357, 2012.

Ziegler, P. A.: Geological Altas of Western and Central Europe, 239 pp., Shell Int. Pet. Maatschappij, Geol. Soc. Publ. House, Bath, UK, 1990.